208
6/8/87 JS ⑤ I-30186 DR 0250-X

ANL-87-6

Chemical Technology
Division
Chemical Technology
Division
Chemical Technology
Division
Chemical Technology
Division
Chemical Technology
Division
Chemical Technology
Division
Chemical Technology
Division
Chemical Technology
Division
Chemical Technology
Division
Chemical Technology
Division
Chemical Technology
Division
Chemical Technology
Division
Chemical Technology
Division
Chemical Technology
Division
Chemical Technology
Division
Chemical Technology
Division
Chemical Technology
Division

Investigation of Primary Li-Si/FeS_2 Cells

by L. Redey, J. A. Smaga, J. E. Battles,
and R. Guidotti

Argonne National Laboratory, Argonne, Illinois 60439
operated by The University of Chicago
for the United States Department of Energy under Contract W-31-109-Eng-38

Chemical Technology
Division
Chemical Technology
Division
Chemical Technology
Division
Chemical Technology
Division

DISTRIBUTION OF THIS DOCUMENT IS UNLIMITED

Argonne National Laboratory, with facilities in the states of Illinois and Idaho, is owned by the United States government, and operated by The University of Chicago under the provisions of a contract with the Department of Energy.

Printed in the United States of America
Available from
National Technical Information Service
U. S. Department of Commerce
5285 Port Royal Road
Springfield, VA 22161

NTIS price codes
Printed copy: A04
Microfiche copy: A01

Distribution Category:
Energy Storage--Electrochemical--
Advanced Batteries (UC-94cb)

ANL--87-6

DE87 010243

ANL-87-6

ARGONNE NATIONAL LABORATORY
9700 South Cass Avenue
Argonne, IL 60439

INVESTIGATION OF PRIMARY Li-Si/FeS_2 CELLS

by

L. Redey, J. A. Smaga, and J. E. Battles

Chemical Technology Division

and

R. Guidotti

Sandia National Laboratories
Battery Development Division
Albuquerque, NM 87185

April 1987

TABLE OF CONTENTS

LIST OF FIGURES

LIST OF FIGURES (contd)

LIST OF TABLES

INVESTIGATION OF PRIMARY Li-Si/FeS_2 CELLS

by

L. Redey, J. A. Smaga, R. Guidotti,* and J. E. Battles

ABSTRACT

The factors that limit the performance of thermally activated Li-Si/FeS_2 batteries were defined through the use of electrochemical characterization tests and post-test examinations. For the characterization tests, 82 individual cells were instrumented with multiple voltage sensors and discharged under isothermal and isobaric conditions. The voltage data for the sensors were recorded to determine the ohmic and electrochemical impedances of each cell component at different levels of discharge. The data analysis completed to date has demonstrated that this approach can successfully differentiate the influence of various operating parameters (e.g., temperature, current density), electrode structures (e.g., FeS_2 particle size), and additives on cell capacity, specific energy, and power capability. Thirty cells selected from these tests and additional tests at SNL were examined using optical and scanning electron microscopy, energy dispersive spectroscopy, and X-ray diffraction. These analyses documented microstructural and compositional changes in the active materials and electrolyte. In general, the electrochemical impedance of the FeS_2 electrode limited cell performance. Several methods (including use of fine FeS_2 particle size, graphite additions, and higher operating temperatures) produced measurable reductions in this impedance and yielded significant improvements in specific energy and power. Additions of KCl to the negative electrode extended the low-temperature capacity of this electrode by counterbalancing gradients in electrolyte composition that develop during discharge.

---

*Sandia National Laboratories, Albuquerque, NM.

EXECUTIVE SUMMARY

Individual cells constitute the fundamental electrochemical units used in the construction of the bipolar type of Li-Si/FeS_2 thermal battery. Studies were conducted on single cells, operated under isothermal and isobaric conditions, to identify the variables that limit their performance and to determine ways of extending the usable cell capacity and increasing cell power. The experimental methodology included both electrochemical characterization of test cells and their electrodes during discharge and post-test microstructural examination of fully or partly discharged cells. The integration of these two methods has proven effective in elucidating the discharge kinetics of these primary cells. This report discusses the progress made in these investigations.

The electrochemical characteristics of a cell and its electrodes were determined by a set of five voltage sensors inserted at different locations within the cell. The potential changes measured by these sensors during galvanostatic-discharge current interruptions and high-intensity current contact pulses were converted into values that described electrode impedance as a function of the depth of discharge and changes in cell-component composition. The findings indicated that the positive electrode develops a high impedance that limits cell power, capacity, and energy. High temperatures, fine FeS_2 particle size, and graphite additions to the positive electrode reduced the observed impedance. Of the tested additives to the positive electrode, graphite produced a significant improvement. Addition of KCl to the negative electrode increased the available cell capacity at low temperatures ($\lesssim$400°C).

The series of morphological and compositional changes that occurred within a cell during discharge were determined by optical and scanning electron microscopy, energy dispersive spectroscopy, and X-ray diffraction. These post-test analyses were conducted on selected cells from our characterization studies, as well as additional cells tested at Sandia National Laboratories. Most of the observed microstructural variations between these groups of cells were due to differences in initial separator thickness and the pressure applied to the cells. Thicker separators and increased mechanical load on the cell increased the quantity of electrolyte within the electrodes, especially the positive electrode. The higher electrolyte content, in turn, reduced reaction gradients within the electrodes, especially in the FeS_2 electrode.

In addition to continuing the analysis of the generated data, recommendations are made (1) to expand the studies of positive-electrode additives, (2) explore methods of increasing the electrolyte content and uniformity within the cell components (during discharge), and (3) to determine the relevant range of applied pressures experienced in actual thermal batteries. Finally, the Integrated Measuring and Modeling Method developed at Argonne National Laboratory should be considered as a means of optimizing Li-Si/FeS_2 cell performance.

1 INTRODUCTION

This document reports on the work performed between September 30, 1985, and February 28, 1986, under contract SNL 64-9979, which is aimed at investigating the electrochemical performance of primary Li-Si/FeS_2 cells and their electrodes. This report is based on an interim report of February 1986.[1] The work in this period has been concentrated in two areas of investigation: (1) the electrochemical performance of the cell and electrodes and the effect that design and operating variables have on it, and (2) the composition and morphological changes of the cell during discharge. The overall objective is to better understand the performance limitations of the cell system. The work completed before September 30, 1985, under the specified contract with Sandia National Laboratories (SNL) was reported elsewhere.[2]

In electrochemical characterization studies, investigations were conducted (1) to determine the voltage losses that occur in cell components and (2) to find exactly where voltage losses that limit cell performance occur in the cell and the effect various parameters have on such losses. These losses result from electrochemical impedances and ohmic resistances in the electrode beds and separator, as well as from ohmic losses in the electronic cell components. Parameters investigated in these studies included electrode and electrolyte composition, FeS_2 particle size, temperature, current density, and mechanical load.

Post-test examinations were directed towards determining the dimensional stability of the cell components and the compositional changes occurring within these components. The purpose of this work was to determine how the general structure of the cell changes during discharge and to correlate variations in the observed microstructures with different cell design, cell performance, and operating conditions.

2 ELECTROCHEMICAL CHARACTERIZATION STUDIES

2.1 Cell Components and Experimental Conditions

The cell components used in these studies were fabricated at SNL. The most important physical and chemical characteristics of the investigated cell components are summarized in Table 1. An SNL cell tester was used for our studies. To achieve *in situ* cell assembling capability and improve heat management during the test, a mounting stage was built to accept and firmly fix the current and voltage leads, as well as a thermocouple for monitoring cell temperature. In conjunction with a novel jig, this stage permits very precise assembly of the cell, with no more than ±0.1-mm misalignment of the components, in a helium-atmosphere glove box on the tester. The cell-component containers received from SNL were opened in the glove box, and the cell components were never exposed to other than a pure helium atmosphere. Currently, a heat-insulation layer about 10-mm thick is wrapped around the cell perimeter and on the back face (the side farthest from the cell) of the BN heater blocks to ensure more-uniform temperature distribution in the cell sandwich. After a few weeks of operation, severe jamming of the mechanical-load bar in the guiding sleeves occurred, probably because of friction-induced wear between the metal components in the high-purity helium atmosphere of the glove box. The problem was eliminated by repolishing the load bar and applying high-vacuum silicone grease on the sliding surfaces.

2.1.1 Electrochemical Test Procedure

The cells were investigated under galvanostatic discharge conditions. The discharge program, which includes interruptions and/or superimposed current pulses, is executed by a special current source with automatic or manual control. The measuring technique of voltage loss is described in more detail in Ref. 3. The measured data are stored on magnetic disk for later data processing and analysis.

2.1.2 Test Cell Configuration

The following list describes the sequence of the components in the test cell sandwich (the components are listed from top to bottom):

(1) Copper assembly plate, heat distributor, 3-mm thick.

(2) Mica electrical insulator sheet, 0.125-mm thick.

(3) Molybdenum current collector plate, 0.42-mm thick, with back-face voltage lead (+BV) and positive current lead.

(4) Positive electrode pellet.

(5) Voltage probe, molybdenum wire, 0.1-mm dia, as front-face voltage lead of the positive electrode (+FV).

(6) Electrolyte pellet with a half-round slot for accepting reference electrode.

(7) Ag/Ag$^+$ reference electrode in a closed-end (1.0-mm OD) Pyrex tube (R), as described in the previous report.[2]

(8) Electrolyte pellet with a half-round slot for accepting the reference electrode.

(9) Voltage lead, same as (5) (-FV).

(10) Negative electrode pellet.

(11) Molybdenum current collector with voltage lead (-BV) and current lead, same as (3).

(12) Mica sheet, same as (2).

(13) Copper assembly plate, same as (1).

In the earlier experiments, a 0.25-mm-OD thermocouple was used between components (2) and (3). In later experiments, the thermocouple was fixed in a hole of the copper assembly plate (13). The following five electrical signals were measured: positive electrode potential (+BV vs. R), negative electrode potential (-BV vs. R), IR voltage drop in the positive electrode bed (+BV vs. +FV), IR voltage drop in the negative electrode bed (-BV vs. -FV), and cell voltage (+BV vs. -BV). The molybdenum current collectors ensured less than 1-mV voltage drop at 1-A/cm^2 current density between the voltage probe BV and any point in the molybdenum current collector/electrode bed interface. Consequently, this arrangement ensured almost perfect one-dimensional current distribution over the faces of the electrodes, i.e., uniform current density in the plane of the electrode/electrolyte interface. The condition of one-dimensional current distribution justifies the applicability of area-specific values, which, in turn, provide useful data for engineering calculations and cell/battery system optimization.

The molybdenum current collector has another advantage over a stainless steel collector in electrode investigation. Namely, it minimizes the intercomponent resistance between the collector and electrode. As we found and reported,[2] the intercomponent resistance is significant, especially between stainless steel and Grafoil. It is a strong function of mechanical pressure applied on the test cell and may vary during the experiment. The area-specific resistance of the Grafoil/stainless steel contact varied between 0.2 and 2.0 ohm·cm^2 when the load was cycled between a pressure of 85 and 5 kPa.

2.1.3 Experimental Conditions

The effects of the following parameters were investigated: particle-size range of FeS_2 (see Table 1); additives in the electrolyte and the electrode mixes (see Table 1); thickness of the positive electrode (see Table 1); temperature (375-550°C); current density of 50-150 mA/cm^2 in galvanostatic discharge and 200-1000 mA/cm^2 in current pulses; mechanical load (6-180 kPa); and discharge pattern (discharge termination point, frequency of current interruptions, and length of pulses). In this report, effects of all parameters except positive-electrode thickness and mechanical load are discussed. The two parameters not dealt with are still under investigation.

Table 1. Characteristics of Cell Components[a]

		Description					
Designation	Function	Comp.	wt %	Weight,[b] g	Thickness, mm	Theoretical Capacity,[c] mAh/cm²	Notes
M-1	Positive electrode pellet, catholyte	FeS_2 purif.	75	1.03	0.43	21.79	-60 + 100 mesh FeS
		EB119B mix	25				
		Grafoil			0.13		
M-3	Positive electrode pellet, catholyte	FeS_2 purif.	75	1.03	0.43	21.79	-170 + 230 mesh FeS
		EB119 mix	25				
		Grafoil			0.13		
M-5	Positive electrode pellet, catholyte	FeS_2 purif.	75	1.03	0.43	21.79	-230 + 325 mesh FeS_2
		EB119B mix	25				
		Grafoil			0.13		
M-4-1	Positive electrode pellet, catholyte, CT162 mix	FeS_2 purif.	75	1.03	0.43	21.79	-325 + 425 mesh FeS_2
		EB118A mix	25				
		Grafoil			0.13		
M-4-2	Positive electrode pellet, catholyte, CT162 mix	FeS_2 purif.	75	2.06	0.86	43.58	-325 + 425 mesh FeS_2
		EB118A mix	25				
		Grafoil			0.13		
M-4-Ni	Positive electrode pellet, catholyte	CT162 mix	90	1.11	0.50	21.79 (as FeS_2)	-325 + 425 mesh FeS_2
		Ni powder	10				
		Grafoil			0.13		
M-4-Gr	Positive electrode pellet, catholyte	CT162 mix	90	1.11	0.50	21.79	-325 + 425 mesh FeS_2
		graphite powder (Lonza KS 44)	10				
		Grafoil			0.13		
XCT174	Positive electrode pellet, catholyte	FeS_2 purif.	75	1.03	0.43	21.79	-425 mesh FeS_2
		EB119B mix	25				
		Grafoil			0.13		

(contd)

Table 1. (contd)

Designation	Function	Description Comp.	 wt %	Weight,[b] g	Thickness, mm	Theoretical Capacity,[c] mAh/cm^2	Notes
EB119B	Separator pellet, electrolyte mix	LiCl-KCl eutectic	65	2.0	1.42	—	With a ref. electrode, 2 slotted separator pellets are used.
		MgO powder	35				
EB172	Separator pellet, electrolyte mix	LiCl-KCl eutectic	60	2.0	1.41	—	With a ref. electrode, 2 slotted separator pellets are used.
		MgO powder	40				
XEB169	Separator pellet, electrolyte mix	LiCl-KCl eutectic	63.34	2.0	1.41	—	With a ref. electrode, 2 slotted separator pellets are used.
		MgO powder	34.11				
		Li_2O	2.5				
XEB194	Separator pellet, electrolyte mix	LiCl-KCl eutectic	62.4	2.0	1.41	—	With a ref. electrode, 2 slotted separator pellets are used.
		MgO powder	33.6				
		Li_2O	4.0				
EB118A	Electrolyte mix	LiCl-KCl eutectic	88	—	—	—	Used in M-4 positives.
		SiO_2 (Cab-O-Sil, EH-5)	12				
F	Negative electrode pellet, standard anolyte	$Li_{3.17}Si$ (Li-Si, 44-56%)	100	1.0	0.89	170.0 (as 100% of Li to Li^+)	-170 + 325 mesh alloy
AM10	Negative electrode pellet	$Li_{3.17}Si$ (same as in F)	90	0.7	0.85	117.0 (as 100% of Li to Li^+)	-170 + 325 mesh alloy
		KCl powder	10				-270 mesh KCl

---

[a] Diameter of cell components is 3.175 cm (1.250 in.). Intercomponent area is 7.917 cm^2.

[b] Pellet weight is given without Grafoil; weight of Grafoil is 0.138 ± 0.12 g/disc.

[c] For $Q_m = 1$, where Q_m is the progression of discharge in faradays per mole of FeS_2.

The discharge was terminated on the basis of three different criteria: (1) at constant Q_m (Q_m is the progression of discharge in faradays per mole of FeS_2; for a complete discharge of FeS_2, Q_m is equal to 4), (2) at the sharp break point on the discharge curve of the positive electrode at the beginning of the lower plateau (see Fig. 1) in coincidence with a similar break point on the cell-voltage curves described in Sec. 2.3.4, and (3) at 1-V cell voltage. Method (1) has not proven to be satisfactory for comparison of cell and electrode performance because it terminates the discharge irrespective of voltage conditions. Method (2) was used in the majority of experiments in which the cell was subjected to post-test microstructural investigation (Sec. 3, Table 7). Method (3) is very useful to get a complete description of the full-discharge capability of the cell beyond the standard 1.5-V cutoff cell voltage. This method allowed us to evaluate energy and power performance in the full available range at any cutoff voltage, in addition to the 1.5-V cutoff voltage.

2.2 Data Analysis Technique

By using a reference electrode and properly placed voltage probes, the electrochemical characteristics of the cell components can be readily measured. Furthermore, time-related investigation of the voltage responses to current pulses or interruptions provides information about the dynamic behavior of the cell and those cell components that are responsible for the observed voltage losses.[3]

Although the electrode potential was measured with respect to a silver reference electrode, it is shown in the figures in this report on the standard Li-Al potential scale. The Li-Al reference electrode, which was introduced by Argonne National Laboratory (ANL) as a potential standard for testing of Li-alloy-containing batteries, uses the α-Al + β-LiAl two-phase alloy.[3] Progression of discharge is expressed as a molar quantity of discharged electricity (Q_m) in faradays per mole of FeS_2. All positive electrode pellets, except M-4-2, had the same area loading: 21.79 mAh/cm^2 in a 1 e^-/FeS_2 process. Consequently, for these electrodes, $Q_m = 1$ represents 21.79 mAh/cm^2. Area-specific values of discharged capacity (ASC) and energy (ASE) are described in units of mAh/cm^2 and mWh/cm^2, respectively, at any specified Q_m.

The ASC and ASE values of several cells are reported in Tables 2-5. Ratios of ASE/ASC, which are the weighted average voltages of cells discharged to the specified cutoff voltage, are tabulated for the same cells. Although ASC, ASE, and ASE/ASC values are reported only for the cutoff condition, a data bank is available to calculate these values for any intermediate cell voltage.

The dynamic behavior of an electrode in an operating cell is characterized by the power-performance-related parameter referred to as the apparent electrochemical impedance (ASI_t). The ASI_t is a strong function of Q_m and t and the properties of the electrode being investigated but is almost independent of current density; ASI_t, in $ohm \cdot cm^2$, is calculated as

$$ASI_t = \Delta\varepsilon/i = (\varepsilon_{inst} - \varepsilon_s)/i \qquad (1)$$

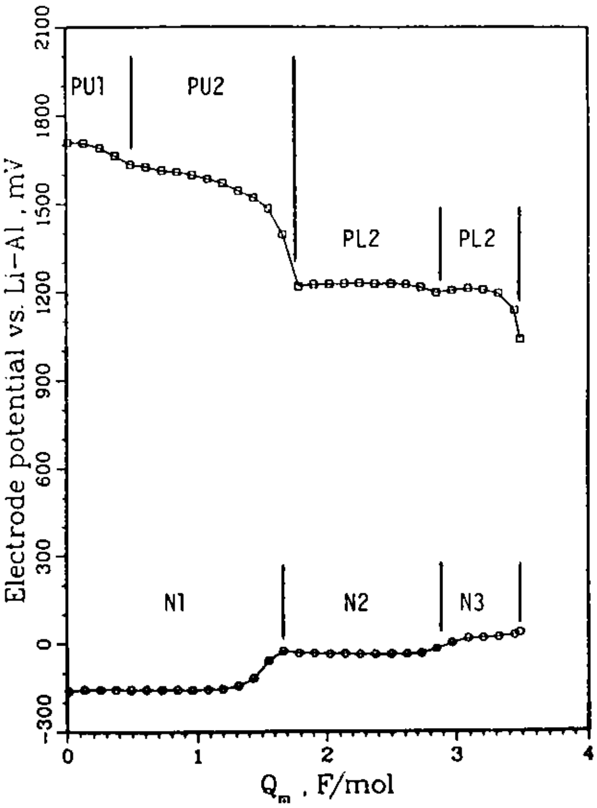

Fig. 1.

Potentials of Electrodes in Cell F/EB119B/M-1. PU1 and PU2 are upper plateaus of the positive electrode; PL1 and PL2 are lower plateaus. N1, N2, and N3 are plateaus of the negative electrode. (Test conditions: 450°C, 50 mA/cm^2, 82.4 kPa, 1-V cell-voltage cutoff).

Table 2. Specific Capacities and Energies of Cells F/M-1 as Function of Temperature and Current Density[a]

Temperature, °C	Current Density, mA/cm^2	ASC, mAh/cm^2	ASE, mWh/cm^2	ASE/ASC
400	50	34.7	59.6	1.72
450	50	34.8	61.0	1.75
450	100	33.2	56.2	1.69
450	150	30.5	47.6	1.56
500	50	36.2	65.1	1.80
500	100	35.5	61.3	1.72
550[b]	50	27.3	50.1	1.83
550	100	36.0	62.9	1.75

[a] Discharge was terminated at 1.5-V cell voltage; each cell had two pellets of the EB119B separator.

[b] Cell test was terminated earlier because of electrolyte extrusion.

Table 3. Performance of Cells Built with Different Positive Electrodes[a]

Electrode	Temperature, °C	Current Density, mA/cm^2	ASC, mAh/cm^2	ASE, mWh/cm^2	ASE/ASC
F/M-1	450	100	33.2	56.2	1.69
F/M-3	450	100	35.0	59.1	1.69
F/M-4-1	450	100	33.0	55.5	1.68
F/M-5	450	100	35.2	60.2	1.71
F/XCT174	450	100	35.5	61.0	1.72

[a] Discharge was terminated at 1.5-V cell voltage.

Table 4. Effect of Additives in Positive Electrodes[a]

Electrode	Temperature, °C	Current Density, mA/cm^2	ASC, mAh/cm^2	ASE, mWh/cm^2	ASE/ASC
F/M-4-1	375	100	9.1	14.2	1.56
F/M-4-Ni	375	100	8.1	12.4	1.53
F/M-4-1	450	100	33.0	55.5	1.68
F/M-4-Ni	450	100	30.1	52.5	1.63
F/M-4-Gr	450	100	34.6	60.8	1.76
F/M-4-1	450	100/200[b]	31.7	52.2	1.65
F/M-4-Ni	450	100/200	30.3	52.0	1.72
F/M-4-Gr	450	100/200	33.2	55.6	1.67

[a] Values are calculated for 1.5-V cell voltage cutoff.

[b] Galvanostatic discharge with 100-mA/cm^2 current density and current pulses of 200 mA/cm^2 for 15 s in every minute.

Table 5. Effect of KCl Additive in Negative Electrodes[a]

Electrode	Temperature, °C	Current Density, mA/cm^2	ASC, mAh/cm^2	ASE, mWh/cm^2	ASE/ASC
AM10/M-4-Ni	375	100	22.1	35.2	1.59
AM10/XCT174	400	100	24.5	40.2	1.64
AM10/XCT174	450	100	30.1	50.1	1.66

[a] Values are calculated for 1.5-V cell voltage cutoff.

where ε is the electrode potential of either the positive or negative electrode in mV, ε_s is the steady-state value prior to current interruption or pulse, ε_{inst} is the instantaneous potential measured at t seconds after the current interruption or initiation of a current pulse, and i is the current density in mA/cm². If the pulse is superimposed on a steady current, i is the difference between the steady and pulse current densities. According to Eq. 1, ASI_t is negative for a positive electrode and positive for a negative electrode. Because the reference electrode is at the half-thickness of the separator, ASI_t includes half the area-specific resistance of the separator. Earlier, we reported the measured resistivity of the electrolyte mix EB119B as a function of temperature (Fig. 1 in Ref. 2). We concluded that 230, 190, and 170 mohm·cm² is included in the ASI_t values at 400, 450, and 500°C, respectively. The sum of the ASI_t values of the positive and the negative electrodes gives the area-specific impedance of the cell sandwich, excluding the effect of the current collectors. The standard interrupt time was uniformly 15 s in these experiments.

The voltage drop across the electrode bed under current flow provides information about the ohmic-type voltage losses. A normalized value of this voltage loss, the area-specific resistance (ASR), is calculated by

$$ASR = (\Delta\phi_i - \Delta\phi_o)/i \qquad (2)$$

where $\Delta\phi_i$ is the potential difference between voltage probes FV and BV under current flow, $\Delta\phi_o$ is the potential difference between the same probes on open circuit, and i is the current density. Unlike ASI_t, ASR is almost independent of the current interruption time.

Primarily ASI_t and, to a lesser degree, ASR control power performance; therefore, they are important characteristics of the battery electrodes and yield useful data for cell design and optimization.

In several experiments, especially at higher temperatures (500-550°C) and mechanical loads (above 90 kPa), the electrolyte paste was extruded to a degree from the cell sandwich during the experiment. A semi-quantitative evaluation of this phenomenon has been attempted by using the estimated area and distribution of the extruded electrolyte layer.

Several cells were subjected to post-test microstructural investigation to find a correlation between electrochemical performance and microstructure or morphological changes. These results are discussed in Sec. 3. The cells were cooled to room temperature in helium by pulling them from the heater block. An exception was Cell PC036, which was fast-quenched between two precooled -150°C copper blocks. The cooling temperature curves of the cells were recorded.

2.3 Results and Discussion

The results from our experiments are only partially discussed here. A full account on the findings cannot be given at this time because additional work is needed to complete the analysis of the acquired data. To date, 82 successful cell testings (in the PC-cell series) have been completed. The generated data bank contains about 250,000 pieces of information.

2.3.1 Discharge Curve Characteristics

Typical discharge curves of the positive and negative electrodes of an Li-Si/FeS_2 cell are shown in Fig. 1. The discharge curve of the positive electrode has four segments: two on the upper plateau (PU1 and PU2) and two on the lower plateau (PL1 and PL2). The discharge curve of the negative electrode has three segments (N1, N2, and N3). Electrodes of all the tested cells showed the same characteristic plateaus. At too high current densities, however, the plateau separation was not so discernible (e.g., PU1 vs. PU2 or PL1 vs. PL2, compare Fig. 9 to Fig. 11). A generally valid threshold of the critical current density cannot be stated; this value depends on the actual electrode composition. Of the identified segments, PU1, PU2, and N1 have importance to the present investigation because they are the only plateaus operative within the limit of the 1.5-V cell-voltage cutoff (SNL-established limit). Segment PU2 is the most important plateau because it represents about 2/3 of the operative capacity range within the 1.5-V cutoff limit and shows very high ASR and ASI_{15s} values compared with the other segments of the curve (see Fig. 2). This pattern of ASI_{15s} variation as a function of Q_m indicates that it is the positive electrode that limits cell performance on two accounts: (1) the potential of the positive electrode and, consequently, cell voltage sharply drop at the end of PU2, and (2) the high values of ASI_t and ASR limit the power capability of the electrode and influence the available capacity and energy within the cutoff voltage limit. Consequently, any changes in design and composition that affect the PU2 segment will strongly influence the cell performance. The reason for the high-resistance region is not yet known. The experiment with Cell PC036, which was designed to find an explanation for the phenomenon, has not given a definitive answer. Findings of the post-test investigation on the fast-quenched Cell PC036, whose operation was terminated at the peak resistance of the positive electrode, are described in Sec. 3.

2.3.2 Effect of Temperature

Figure 3 shows that the resistance for segments PU1 and PU2 decrease as temperature is increased. This effect is especially significant in segment PU2. Separation between segments PU1 and PU2 was approximately at $Q_m = 0.5$; separation between segments PU2 and PL1 was $Q_m = 1.7$. At high temperatures ($\geq$500°C), the available area-specific capacity and, to an even greater extent, area-specific energy were higher than those at 400-450°C, as shown in Table 2. This temperature effect is reflected in the ASE/ASC ratios. Also shown is the effect of current density on cell performance. Increasing current density decreases ASC, ASE, and the ASE/ASC ratio. The data in Table 2 confirm expected trends in the effects of temperature and current density.

2.3.3 Effect of FeS_2 Particle Size

Analysis of the electrode potential, ASI_{15s}, and ASR data showed that the size range of the FeS_2 particles in the catholyte mix has an important effect on energy, power, and capacity. The variation of the ASI_{15s} values as a function of particle size is shown in Fig. 4. Two important effects are illustrated in this figure. The peak of the ASI_t vs. Q_m plot is lower when the FeS_2 particles are smaller, and the high-resistance section of the curve

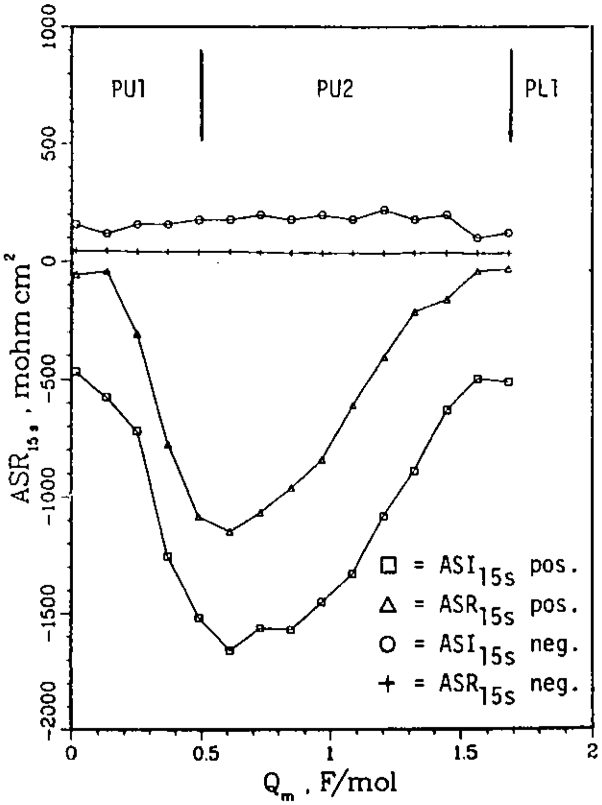

Fig. 2.

Resistances and Electrochemical Impedances in F/EB119B/M-1 Cell. (Test conditions: 450°C, 50 mA/cm², cutoff at break point.)

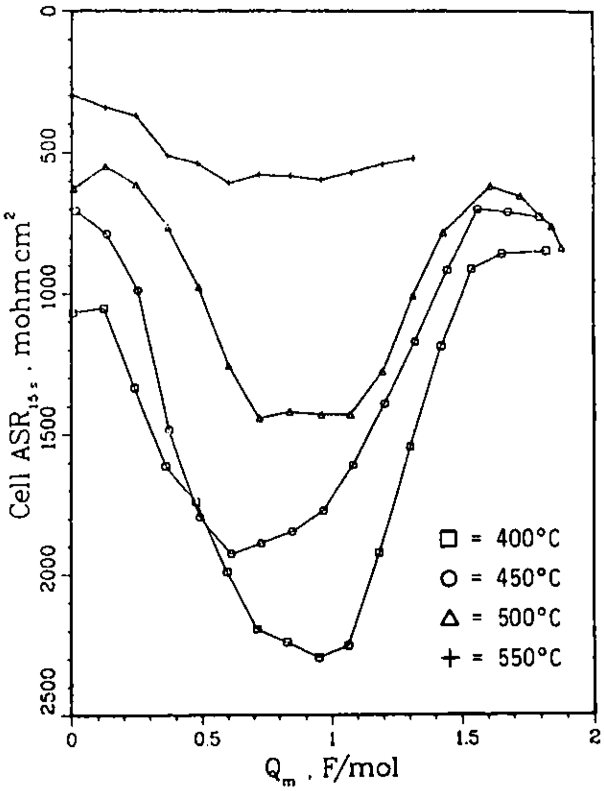

Fig. 3.

The Effect of Temperature on Electrochemical Impedance (ASR_{15s}) of Cell F/EB119B/M-1 (Pressure: 82.4 kPa.)

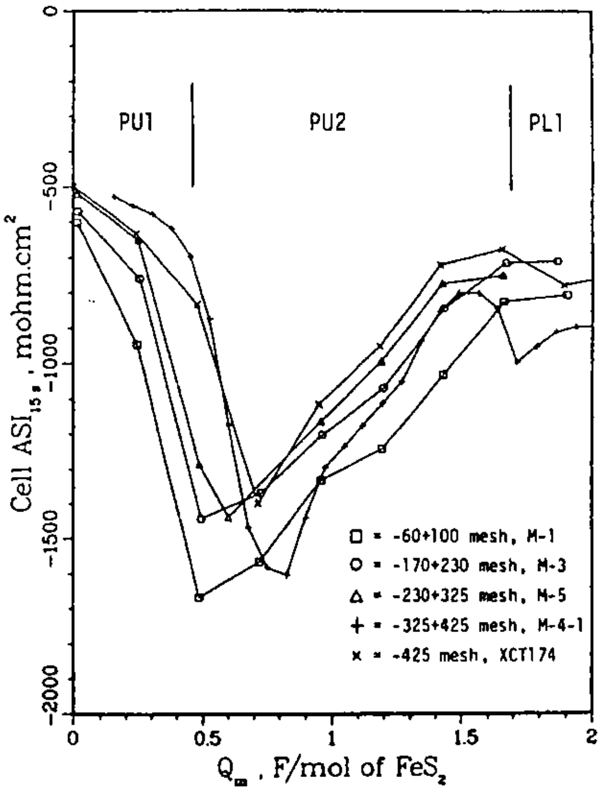

Fig. 4.

The Effect of FeS_2 Particle Size on Electrochemical Impedance in F/EB119B/FeS_2 Cell. (Pressure: 82.4 kPa.)

is shorter, starts later, and ends earlier. The M-4-1 electrode is an exception. Although the M-4-1 positive electrode has marginally better performance in segment PU1 than the other electrodes, its performance in segment PU2 is poorer, as shown by the relatively high and broad ASI_t peak. Neither the ASI_t (Fig. 4) nor the capacity and energy values (Table 3) meet expectations based solely on particle size, which would place the performance level of this electrode between types M-5 and XCT174. This deviant behavior of the M-4-1 electrode, which indicates the high sensitivity of the applied measuring technique, is attributed to the difference in electrolyte-mix composition of this electrode and the other tested positive-electrode pellets (see Table 1). The effect of particle size on dischargeable capacity and energy is shown in Table 3. In the order of the decreasing size of FeS_2, the electrodes have increasing ASC, ASE, and ASE/ASC values, F/M-4-1 being the only exception.

The effect of FeS_2 particle size on electrode potential is shown in Fig. 5a. The plot of the M-4-1 electrode (prepared with -325 + 425 mesh-size FeS_2 powder) is omitted from this figure because of its deviant behavior.

2.3.4 Effect of Current Density

The effect of current density on the potential of the M-1 positive electrode (-60 + 100 mesh FeS_2) is indicated in Fig. 5b. Because of the high ASI in segment PU2, increasing the current density decreases the electrode potential and, thereby, the electrode performance. In Fig. 5c, for the sake of comparison, the discharge potential curves of the other positive electrodes (M-3, M-5, and XCT174), measured at 100-mA/cm² current density, are included along with the plots of the M-1 electrode.

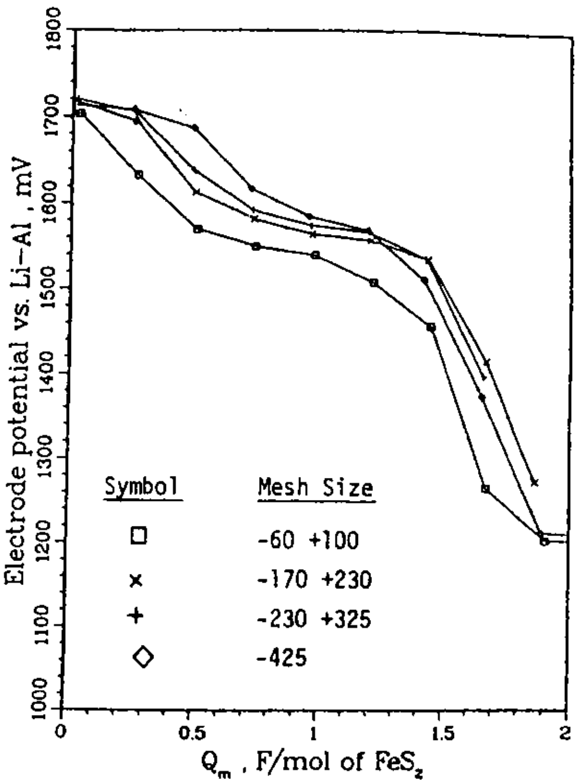

Fig. 5a.

Potentials of FeS_2 Electrodes as Function of Q_m and Particle Size for F/EB119B/FeS_2 Cells. See Table 1 for relationship between mesh size and electrode designation. (Test conditions: 100 mA/cm², 450°C, 82.4 kPa.)

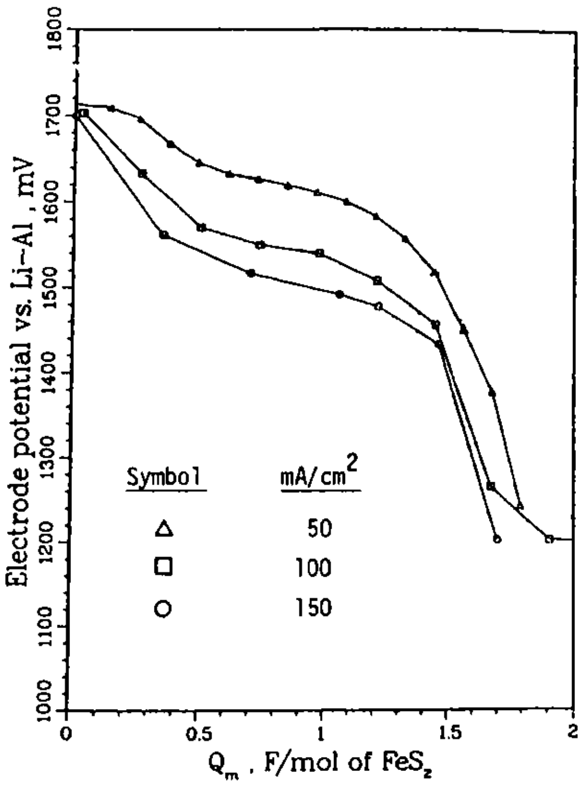

Fig. 5b.

Potentials of FeS_2 Electrodes as Function of Q_m and Discharge Current Density for F/EB119B/M-1 Cells. (Test conditions: 450°C, 82.4 kPa.)

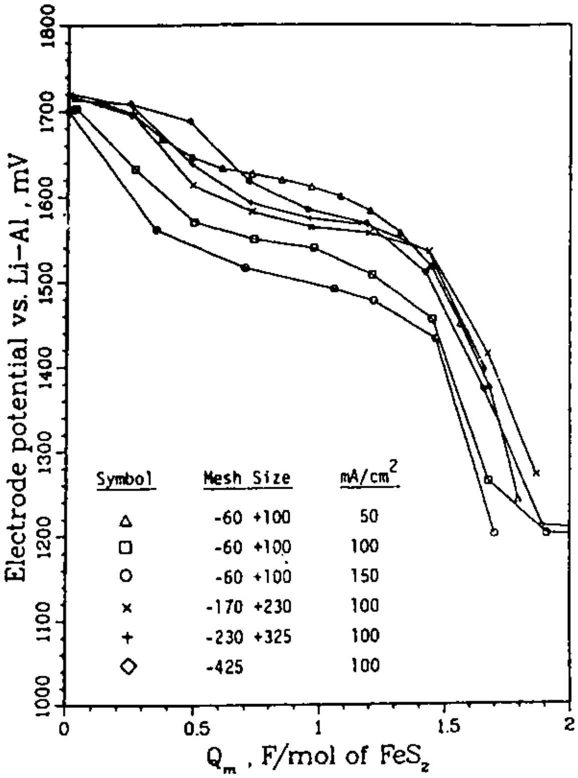

Fig. 5c.

Potentials of FeS$_2$ Electrodes as Function of Q_m and Discharged Capacity for F/EB119B/FeS$_2$ Cells. This figure is a combination of Figs. 5a and 5b. (Test conditions: 450°C, 82.4 kPa.)

2.3.5 Effect of Additives

We also studied the effects of adding graphite or nickel powder to the positive electrode and KCl to the negative electrode. Results of the present tests performed on the SNL-prepared pellets (M-4-Ni and M-4-Gr, see Table 1) have proven the beneficial effect of the graphite additive. The nickel additive would improve power only in high-intensity power pulses.

Figure 6 shows the ASI$_{15s}$ values of the M-4-Ni and M-4-Gr positive electrodes. Electrode M-4-1 is also included to represent an electrode without additive. Graphite and, to an even greater extent, nickel decreases the electrochemical impedance in segments PU2, PL1, and PL2; the greatest improvement is seen in segment PU2.

The discharge curves of the positive electrodes are shown in Fig. 7a. Each electrode displays a different pattern of potential change during the progression of discharge. The differences can be explained as follows. The electrode M-4-1 curve in segment PU2 shows the ASI peak characteristic of the other FeS$_2$ electrodes without an additive (see Fig. 4). Nickel (M-4-Ni) is a better electronic conductor and, hence, is expected to have a greater impact on electrochemical performance than graphite (M-4-Gr), but its effect is not without shortcomings. The nickel additive, indeed, decreases electrode impedance, but it also shortens segment PU2 because it reacts with FeS$_2$, forming a lower-activity sulfide and reducing the electrode capacity in the upper plateau range. This capacity, however, is transferred to the lower plateau

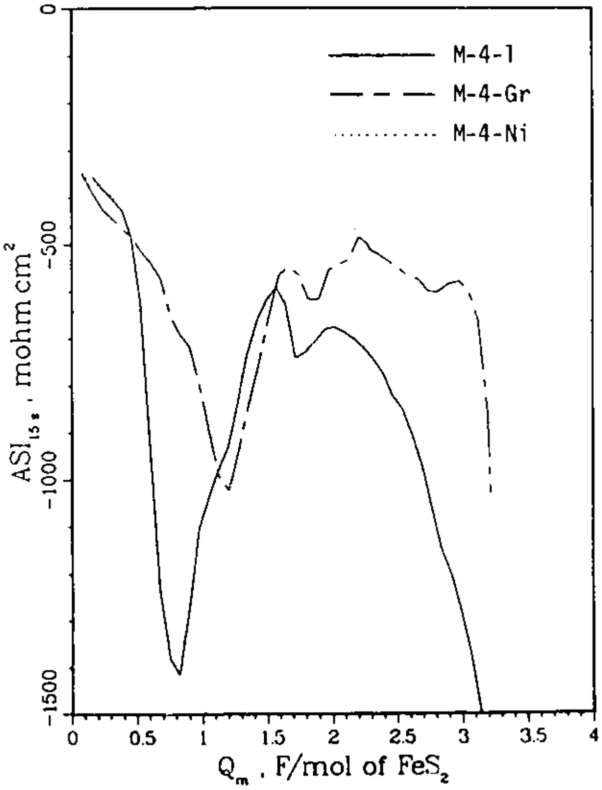

Fig. 6.

Electrochemical Impedances of Positive Electrodes for F/EB119B/FeS$_2$ Cells as Functions of Discharged Capacity and Additive Material. (Test conditions: 450°C, 82.4 kPa, 1-V cutoff, 100 mA/cm^2.)

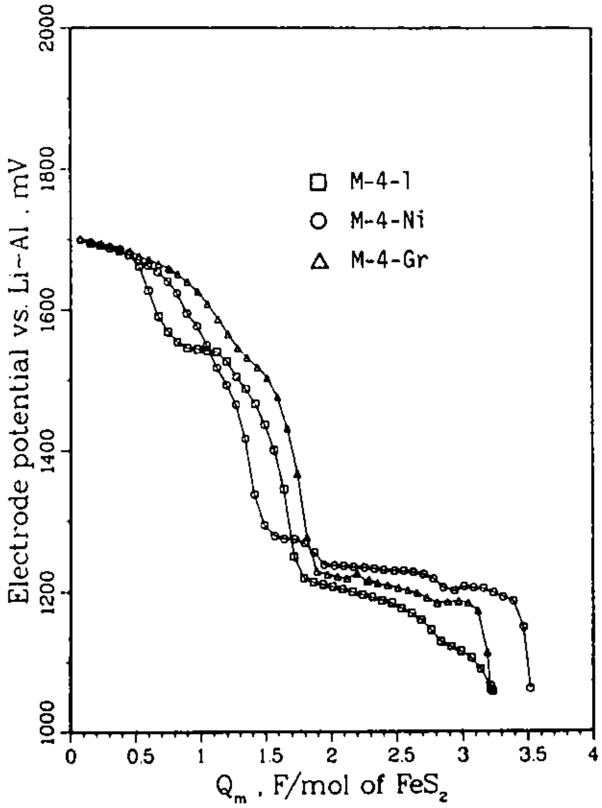

Fig. 7a.

Effect of Additives on Electrode Potential. Same electrodes as in Fig. 6. (Test conditions: 100 mA/cm^2, 450°C, 82.4 kPa, 1-V cutoff.)

sections, as shown by the extended capacity range (compare curves for M-4-Ni and M-4-1 in Fig. 7a). The graphite additive reduces electrode impedance in segments PU2 and PL1 and increases active material utilization, thereby extending the capacity in the upper plateau.

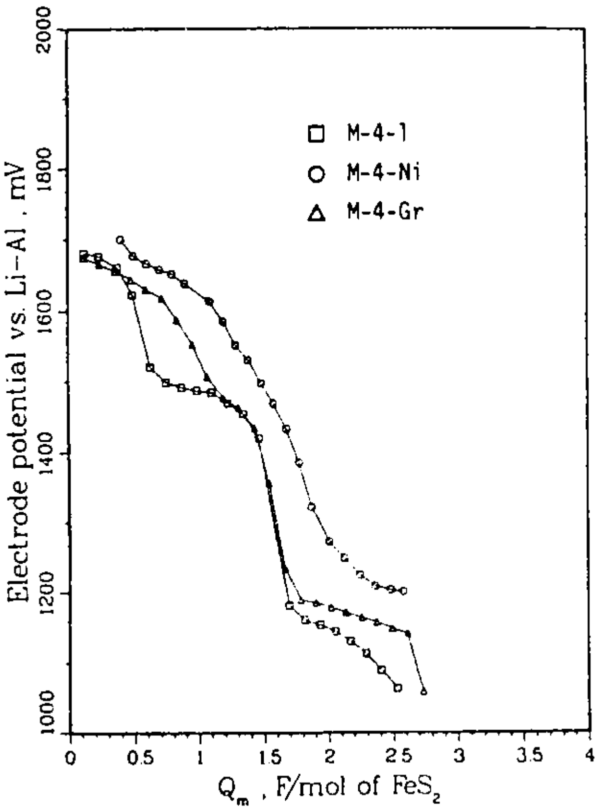

Fig. 7b.

Potentials of M-4-Type Electrodes at the End of 200-mA/cm^2 Current Pulses Superimposed on 100-mA/cm^2 Discharge. (Test conditions: 450°C, 83.4 kPa.)

Potentials of the M-4-type electrodes at the end of 200-mA/cm^2 current pulses of 15-s duration superimposed on the 100-mA/cm^2 discharge are plotted in Fig. 7b.

Potentials for 100-mA/cm^2 discharges and at the end of 200-mA/cm^2 current pulses are plotted for M-4-1 in Fig. 8, M-4-Ni in Fig. 9, and M-4-Gr in Fig. 10. The extent of the increase of polarization (the difference between the potentials on the two curves in each figure at any Q_m) when the electrode is being pulsed is in accordance with the ASI variation pattern of the three types of electrodes, i.e., the potential difference is proportional to the ASI at any Q_m. Discharge curves of the three cells built with different M-4-type positive electrodes and identical negative-electrode (F) and electrolyte (EB119B) pellets show the improved capacity produced by the M-4-Gr electrode (Fig. 11).

The ASC, ASE, and ASE/ASC values of cells assembled with different M-4-type electrodes are compared in Table 4. The beneficial effect of the graphite additive at 450°C is striking, especially in the ASE and ASE/ASC values. Pulsing does not significantly affect the available capacity. It is

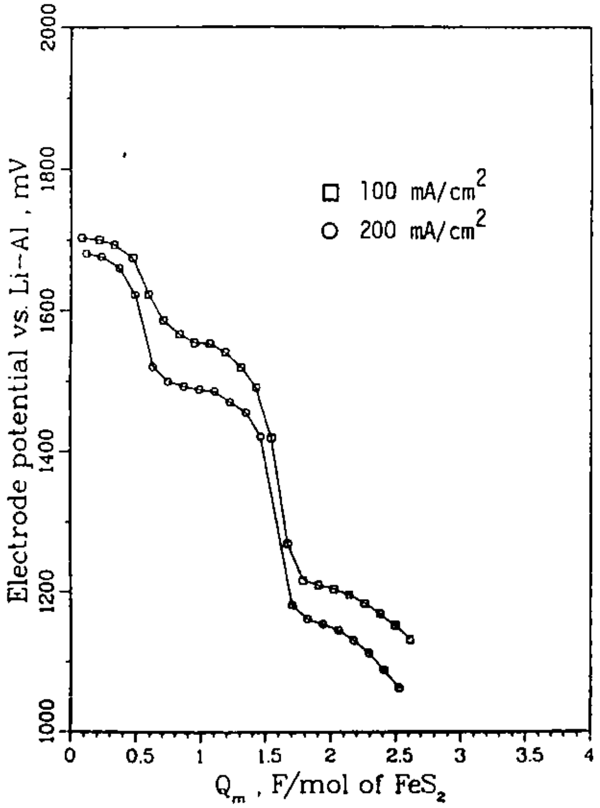

Fig. 8.

Potential of M-4-1 Electrode as Function of Discharged Capacity in Galvanostatic Discharge with 100-mA/cm^2 Current Density and at the End of 15-s, 200-mA/cm^2 Current Pulses. (Test conditions: 450°C, 82.4 kPa.)

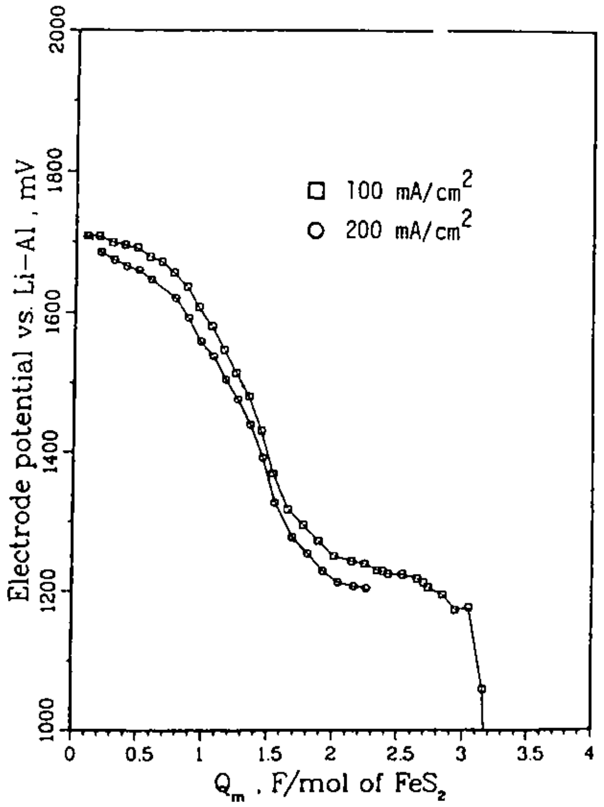

Fig. 9.

Potential of M-4-Ni Electrode as Function of Discharged Capacity in Galvanostatic Discharge with 100-mA/cm^2 Current Density and at the End of 15-s, 200-mA/cm^2 Current Pulses. (Test conditions: 450°C, 82.4 kPa.)

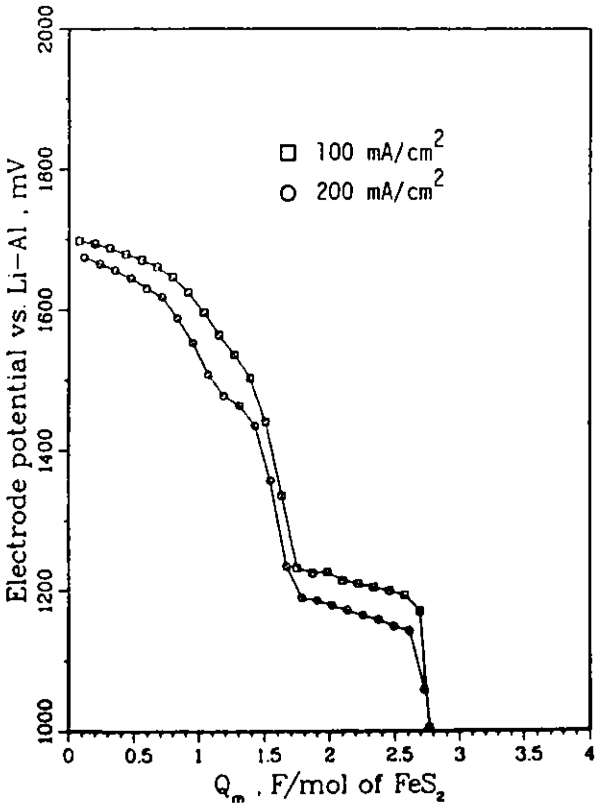

Fig. 10.

Potential of M-4-Gr Electrode as Function of Discharged Capacity in Galvanostatic Discharge with 100-mA/cm² Current Density and at the End of 15-s, 200-mA/cm² Current Pulses. (Test conditions: 450°C, 82.4 kPa.)

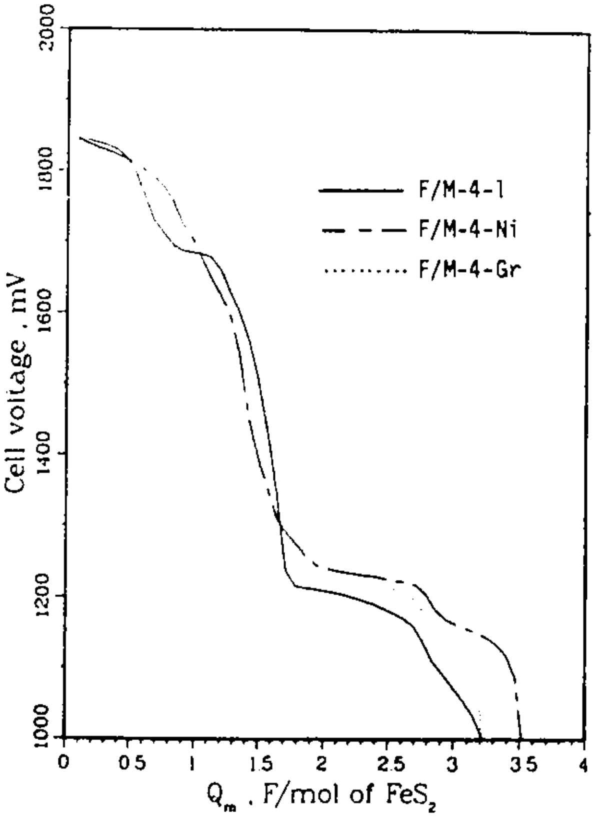

Fig. 11.

Effect of Additives on Cell Voltage. Same electrodes as in Fig. 6. (Test conditions: 100 mA/cm², 450°C, 82.4 kPa, 1-V cutoff.)

interesting to note that the nickel additive increases the power performance to a greater extent than does the graphite additive. At 375°C, the electrodes show poor performance.

The effect on cell performance of KCl electrolyte additive to the negative electrode was studied on cells built with AM10 negative electrodes. This electrode increased the available cell capacity to a great extent at low temperatures: cells assembled with the AM10 electrode operated well at 375°C, as shown in Fig. 12, whereas cell duplicates with the regular negative electrode (F in Table 1) had very poor performance at this temperature (Table 5). At this low temperature, the Li-Si electrode limits cell performance, as shown by the excessive polarization of the negative electrode relative to that of the positive electrode (Fig. 12). At higher temperatures, however, the advantage of the AM10 negative electrodes was not observed (Fig. 13). Figure 13 also shows that the characteristic segments N_1, N_2, and N_3 are shorter with AM10 negative electrodes than with F negative electrode pellets, indicating a lower available capacity and energy. This finding is in reasonable agreement with the theoretical capacities of the F and AM10 negative electrodes (Table 1). Table 5 shows the ASC, ASE, and ASE/ASC values of two types of cells built with AM10 negative electrodes. The beneficial effect of the KCl additive on the performance at low temperature (375°C) is striking when cells F/M-4-Ni and AM10/M-4-Ni are compared in Tables 4 and 5, respectively.

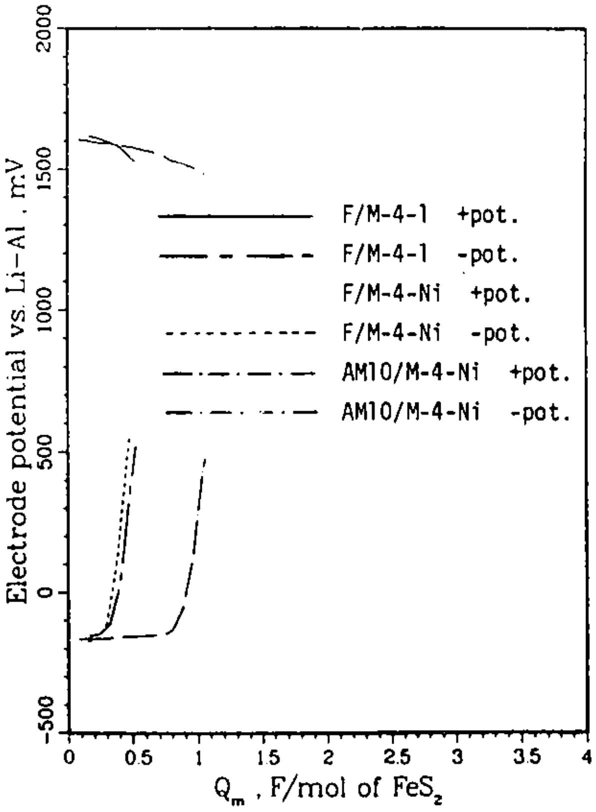

Fig. 12.

Effect of KCl Additive in Negative Electrode. (Test conditions: EB119B electrolyte, 100 mA/cm², 375°C, 82.4 kPa, 1-V cutoff.)

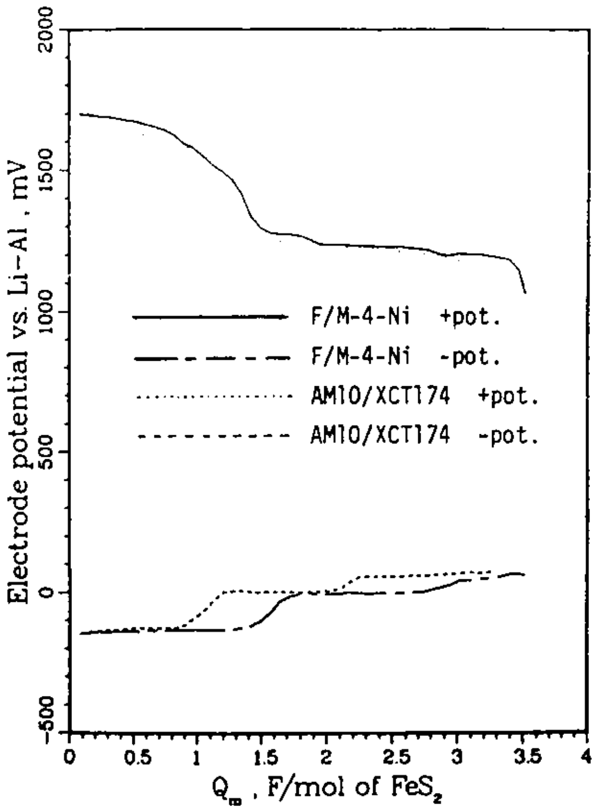

Fig. 13.

Potentials of Negative and Positive Electrodes in Cells F/M-4-Ni and AM10/XCT174. In both cells, EB119B electrolyte was used. (Test conditions: 100 mA/cm², 450°C, 82.4 kPa, 1-V cutoff.)

2.4 Conclusions

We conclude from the results of the electrochemical measurements that

1. the potential, ASI_t, and ASR values of electrodes and their variations under differing conditions are sensitive indicators of the electrochemical properties of the electrodes and the cell;

2. these values provide a firm basis for understanding electrode behavior and the relationships among the various performance parameters and electrode structures;

3. the effect of additives on cell performance can be quantified by the method used in these studies; and

4. the area-specific performance values derived from measurements made under one-dimensional current distribution can be used in cell modeling and other engineering calculations to predict cell performance under various discharge conditions.

3 POST-TEST CELL EXAMINATIONS

The post-test examinations of LiSi/FeS_2 primary cells augment the electrochemical characterization studies by establishing a microstructural foundation for interpreting the observed electrochemical performance. The cumulative data from these examinations also serve to quantify the influence of cell design and operating parameters on the dimensional stability of the different cell components, as well as the composition and distribution of active materials and electrolyte within these components. These parameters include: temperature, discharge current density, depth of discharge, applied pressure, starting component thickness, and active material particle size. In addition, many phenomena, such as Li_2S and iron migration into the separator, were uncovered during these comprehensive examinations.

3.1 Analysis Procedures

The post-test glove-box facility with pure helium atmosphere shown in Fig. 14 made these examinations possible. This facility was originally designed for the examination of LiAl/FeS_x secondary cells and has been described in detail elsewhere.[4,5] Basically, the large glove box houses all the equipment required for the preparation of air-sensitive samples. The smaller glove box is linked with the larger one and contains a metallograph for initial microscopy. Subsequent samples can be prepared in this facility and transferred to other instruments with little or no exposure to air. For these examinations, extensive powder X-ray diffraction (XRD) and scanning electron microscopy-energy dispersive spectroscopy (SEM-EDS) analyses were conducted.

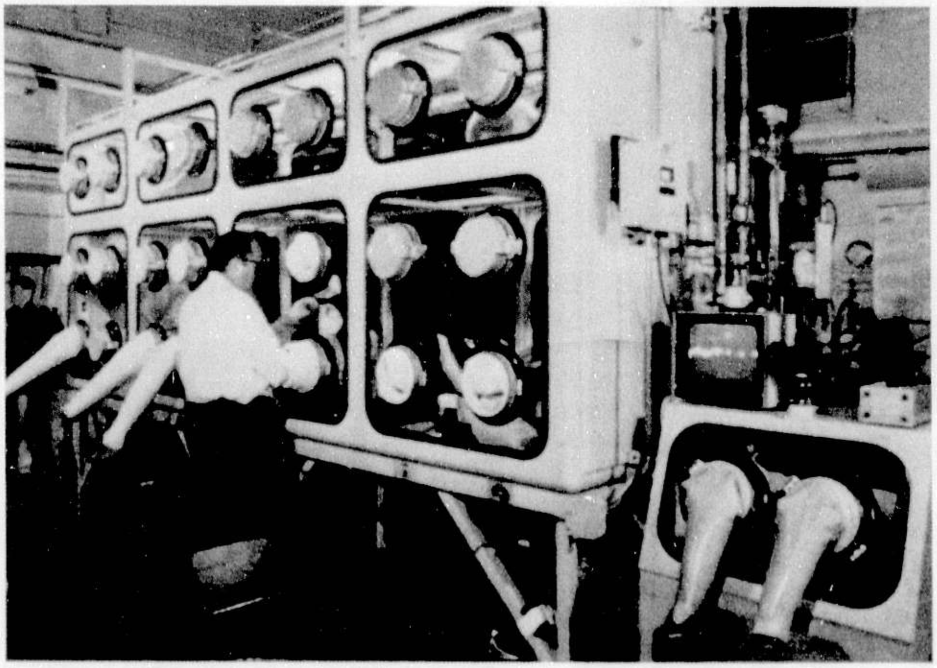

Fig. 14. Post-Test Analysis Facility (where sample preparation and microscopic examination of air-sensitive cell sections are made).

The cells examined during this report period were classified in two main groups. One group consisted of 24 discharged cells that were built and tested at SNL. The designations for these cells began with M1, 162 or OC. With a few exceptions, these cells used identical components. Reported thicknesses of the negative electrodes, separators, and positive electrodes were 0.91, 0.70, and 0.46 mm, respectively. Additional information reported for these cells is presented in Table 6. The second group consisted of 11 cells selected from the PC series built and tested at ANL. The primary physical difference between these cell groups was that the separators used for the PC (and 162) cells were approximately four times thicker to accommodate reference electrodes. The cell components used in the PC series are listed in Table 1, and the operating conditions of the post-tested cells are summarized in Table 7.

3.2 Dimensional Changes

Dimensional changes, especially in thickness, for a single cell have a multiplicative effect when cells are stacked together to form a battery. The thicknesses of each cell and its component parts, positive electrode, separator, and negative electrode, were measured to provide baseline information on the magnitude of these changes as an aid to future battery design. The microscopic measurements were made at multiple locations on a diametrically sliced cell section and averaged to obtain the average thickness change for each component. Comparison of the thickness changes among different cells or cell subgroups identified trends related to the test parameters. Not unexpectedly, the depth of discharge and the pressure applied to maintain good contact between cell components were the major determinants of dimensional change.

3.2.1 The SNL Cells

Table 8 summarizes thickness data for the M1, OC, and 162 cells. Changes in thickness are expressed both as the difference between the final and initial values and as a percentage of the reported initial value. The effect of increasing discharge depth can be seen graphically in Fig. 15, which incorporates data for cells of identical construction: the two OC cells and most of the M1 cells. The positive electrodes showed the largest thickness change. The initial heatup caused a sizeable gain in thickness, and this expansion continued as the cells were discharged. The magnitude of positive-electrode expansion was too large to be offset by decreases in the separator and the negative-electrode thickness once the discharge, Q_m, progressed beyond 0.2 F/mol. As a result, this group of cells showed a trend of increasing thickness with increasing depth of discharge, which closely tracked the curve for positive-electrode expansion.

The expansion of the positive electrodes was related to the formation of low-density discharge products, which are discussed in Sec. 3.3.1. Image analysis of these positive electrodes showed that the volume fraction of active material ranged from 31 to 38 vol %, with no apparent trend related to the degree of discharge. This observation suggested that the discharge phases expanded the electrode structure without causing any significant increase in the volume fraction of solid phases. The different current densities (12.6, 25.3, 50.5, 63.1, and ~75 mA/cm^2) and the two test temperatures (400 and

Table 6. Test Parameters for the M1, OC, and 162 Cells

Cell Number	FeS_2 Sieve Size	Temperature, °C	Discharge (Q_m), F/mol	Current Density,[a] mA/cm^2
OC-400[b]	-60 + 100	400	0.000	0.0
M1-03	-60 + 100	400	0.750	12.6
M1-05	-60 + 100	400	0.749	25.3
M1-12	-60 + 100	400	0.750	50.5
M1-13	-60 + 100	400	0.895	50.5
M1-02	-60 + 100	400	1.501	12.6
M1-04	-60 + 100	400	1.483	25.3
M1-19[c]	-60 + 100	400	1.501	25.3
OC-500[b]	-60 + 100	500	0.000	0.0
M1-21	-60 + 100	500	0.375	75.0
M1-20	-60 + 100	500	0.418	50.5
M1-08	-60 + 100	500	0.750	12.6
M1-07	-60 + 100	500	0.750	25.3
M1-11	-60 + 100	500	0.751	50.5
M1-16	-60 + 100	500	0.751	75.8
M1-15	-60 + 100	500	1.457	75.8
M1-09	-60 + 100	500	1.501	12.6
M1-06	-60 + 100	500	1.501	25.3
M1-18[c]	-60 + 100	500	1.503	50.5
M1-10	-60 + 100	500	1.501	50.5
M1-14	-60 + 100	500	1.501	63.1
M1-17	-60 + 100	500	2.729	75.0
162-18[d]	-325 + 425	400	1.316	50.5
162-19[d]	-325 + 425	500	1.981	50.5

[a] The listed current densities are steady-state values. Current pulses at twice these values were applied for five seconds at the end of each minute of discharge.

[b] Held at temperature for one minute prior to cool down.

[c] Used 1.5-g, instead of 0.7-g, negative electrodes.

[d] Separators were four times thicker than those used in the M1 cells.

500°C) had no discernible influence on the degree of expansion. It should also be recognized that the expansion values listed in Table 8 include the ~0.10-mm thickness of the Grafoil current collector. If the expansion had been based solely on the active material bed, the reported percentages for the electrodes would have been considerably greater. For example, the 87% average increase in positive-electrode thickness for cells discharged to ~0.75 Q_m and the 135% average for cells discharged to ~1.5 Q_m would have been 111% and 173%, respectively (cf. Tables 6 and 8).

Table 7. Test Parameters for the Examined PC Cells

Cell Number	FeS_2 Sieve Size	Temperature, °C	Discharge (Q_m),[a] F/mol	Current Density, mA/cm^2
PC036	-60 + 100	450	0.71	100
PC019	-60 + 100	450	1.80	50
PC035	-60 + 100	450	1.77	50
PC014	-60 + 100	450	1.90	100
PC015	-60 + 100	450	1.70	150
PC009	-60 + 100	450	3.48	50
PC012	-60 + 100	500	1.88	50
PC024	-60 + 100	550	1.31	50
PC026	-170 + 230	450	1.87	100
PC025	-230 + 325	450	1.66	100
PC027[b]	-425	450	1.88	100

[a] With the exception of PC036 and PC009, discharge was terminated at the knee of the discharge curve; see break point between segments PU2 and PL1 in Fig. 1. For PC036, the termination criterion was maximum electrode impedance. For PC009, it was discharged down to 1.0 V.

[b] PC027 was also pulsed at 200 mA/cm^2 during discharge.

For the separators, about two-thirds of the loss in thickness occurred during heatup. The separators from both OC cells lost 0.13 mm, for a 19% reduction from the as-pressed thickness. Experiments conducted at SNL measured the compression of individual separators. Under an applied load of 98.6 kPa, MgO pellets with the same formulation as used in these cells averaged a nearly constant 15% reduction in thickness within minutes after application of the load. The thickness reduction was accompanied by an increase in diameter. A 2-mm increase in diameter was also observed for the separators from these cells. However, a second mechanism, the transport of molten electrolyte to the electrodes, is also possible in actual cells. For the OC and M1 cells, the pressure was less than half (42 kPa) of the pressure used in the tests of individual separators. Therefore, it seems reasonable to conclude that more than one-third of the intial separator compression for the cells was the result of electrolyte movement into the electrodes, especially the negatives because of their ease of wettability.

The additional reduction noted for the discharged cells was typically 0.07 mm, and this decrease was independent of the depth of discharge within the interval of 0.375 to 2.73 Q_m. The mechanism for this decrease was the physical movement of both the MgO powder from the separator and the electrolyte into void spaces along the positive-electrode interface. This mechanical adjustment along the interface occurred during a relatively brief time period and apparently ceased once the solid materials settled into intimate contact.

Table 8. Changes in Cell and Component Thickness for M1, OC, and 162 Cells

Cell	Neg. Elect.		Sep.		Pos. Elect.		Cell	
Number[a]	mm	%	mm	%	mm	%	mm	%
OC-400	+0.01	+1	-0.13	-19	+0.04	+9	-0.08	-4
M1-03	-0.01	-1	-0.21	-30	+0.43	+94	+0.21	+10
M1-05	-0.01	-1	-0.24	-34	+0.31	+67	+0.06	+3
M1-12	-0.02	-2	-0.17	-24	+0.39	+85	+0.20	+10
M1-13	-0.02	-2	-0.18	-26	+0.41	+89	+0.21	+10
M1-02	-0.01	-1	-0.22	-31	+0.67	+146	+0.44	+21
M1-04	-0.02	-2	-0.21	-30	+0.68	+148	+0.45	+22
M1-19	-0.07	-4	-0.22	-31	+0.76	+165	+0.47	+15
OC-500	+0.01	-1	-0.13	-19	+0.07	+15	-0.05	-2
M1-21	-0.01	-1	-0.21	-30	+0.22	+48	0.00	0
M1-20	0.00	0	-0.20	-29	+0.24	+52	+0.04	+2
M1-08	0.00	0	-0.18	-26	+0.45	+98	+0.27	+13
M1-07	0.00	0	-0.16	-23	+0.37	+80	+0.21	+10
M1-16	-0.01	-1	-0.17	-24	+0.37	+86	+0.19	+9
M1-15	-0.02	-2	-0.18	-26	+0.50	+109	+0.30	+15
M1-09	-0.02	-2	-0.18	-26	+0.60	+130	+0.40	+19
M1-06	-0.02	-2	-0.18	-26	+0.59	+129	+0.39	+19
M1-18	-0.08	-4	-0.18	-26	+0.65	+141	+0.39	+19
M1-10	-0.01	-1	-0.20	-29	+0.63	+146	+0.42	+20
M1-14	-0.01	-1	-0.18	-26	+0.45	+98	+0.26	+13
M1-17	-0.01	-1	-0.17	-24	+0.89	+194	+0.71	+34
162-19	+0.01	+1	-0.52	-19	+0.54	+117	+0.03	+1
162-18	-0.01	-1	-0.47	-17	+0.65	+141	+0.17	+4

[a] Tested under an applied load of 42 kPa.

The negative electrodes showed the best dimensional stability. The 0.01-mm (~1%) expansion noted for the OC cells probably resulted from some relaxation of these comparatively dense (~65%) cold-pressed pellets. The discharged cells showed slight reductions in negative-electrode thickness, typically within the range of 0.01 to 0.02 mm. One would expect some loss in thickness during discharge as a result of transport of lithium from the electrode, as well as possible densification caused by sintering. However, the small changes found were at the limit of measurement accuracy, and no clear-cut trend could be established for this group of cells. For cells M1-18 and M1-19, the 4% thickness reductions, which were more than twice the average value, could reflect experimental error in estimating the initial thickness of the 1.5-g electrodes. As with the other cell sections, any effect of test temperature on current density was too small to be resolved from the scatter in the experimental measurements.

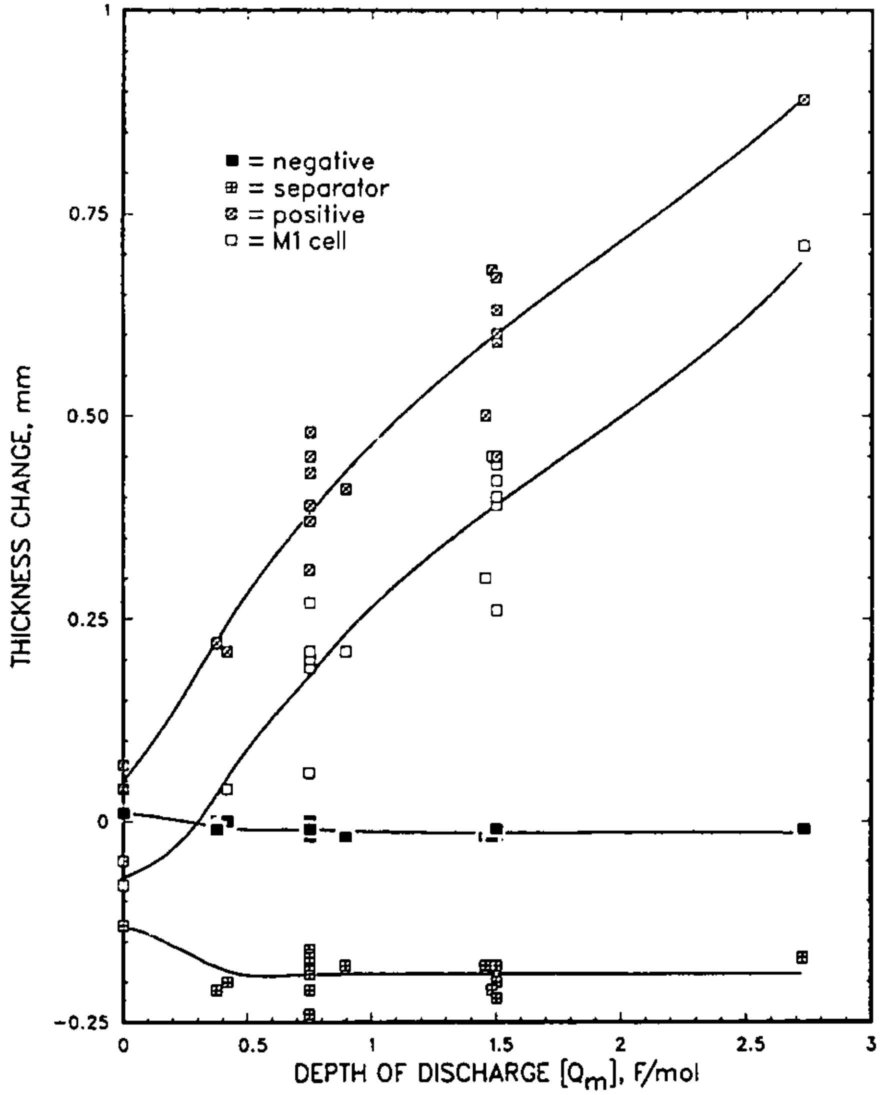

Fig. 15. Changes in Cell and Component Thicknesses as Function of Discharge Level for Cells in the M1 Series

3.2.2 The ANL Cells

In general, the data for the examined PC cells, which are shown in Table 9, paralleled the findings for the M1 series. However, the applied pressure used for these cells was 82.4 kPa, rather than the 42 kPa used for the SNL-tested cells. As a result, the PC cells showed less expansion of the positive electrodes and more compression of the separators and negative electrodes. This observation is illustrated in Fig. 16, in which are plotted the thickness changes for both the PC and 162 cell groups. (Cells 162-18 and 162-19 used components of comparable initial thickness). The greater applied pressure had the largest effect on the thick separators. The PC separators averaged a 0.83-mm (29%) reduction in thickness, which was once again insensitive to depth of discharge. The magnitude of this constant reduction resulted

Table 9. Changes in Cell and Component Thicknesses for PC Cells

Cell Number[a]	Neg. Elect.		Sep.		Pos. Elect.		Cell	
	mm	%	mm	%	mm	%	mm	%
PC036	-0.01	-1	-0.72	-25	-0.42	+91	-0.31	-7
PC019	-0.06	-7	-0.92	-33	+0.50	+109	-0.48	-11
PC035	-0.04	-5	-0.75	-27	+0.56	+122	-0.23	-5
PC014	-0.04	-5	-0.94	-34	+0.72	+157	-0.26	-6
PC015	-0.02	-2	-0.90	-32	+0.62	+135	-0.30	-7
PC009	-0.09	-10	-0.79	-30	+0.84	+182	-0.04	-1
PC012	-0.05	-6	-0.70	-25	+0.58	+126	-0.17	-4
PC024	-0.05	-6	-1.50	-53	+0.39	+85	-1.16	-28
PC026	-0.04	-5	-0.86	-31	+0.60	+130	-0.30	-7
PC025	-0.04	-5	-0.85	-31	+0.56	+122	-1.33	-8
PC027	-0.05	-6	-1.61	-57	+0.57	+124	-1.09	-26

[a]Tested under an applied load of 82.4 kPa.

in overall changes in cell thickness that were negative for each cell in the PC series. The degree of cell compression, however, was still dependent on the discharge level because of the counteracting effect of positive-electrode expansion. The overall cell compression was aided by the reduction in negative-electrode thickness. Unlike the M-1 cells, the degree of this reduction increased with deeper discharges for the PC cells. The marginal reduction in thickness for the M1 cell probably masked this effect.

The PC cells were broken down into subgroups to examine current density, temperature, and FeS_2 particle size. Once again, changes in the first two parameters did not result in a measurable effect. Changes in particle size (cells PC014, PC026, PC025, and PC027) may have influenced the positive-electrode expansion. The small particle sizes seemed to have lessened the degree of expansion by permitting closer packing of the discharge products as they formed. However, the limited data available for this parameter and the inherent scatter measurements of the positive electrode made this conclusion a tentative one.

The applied force that resulted in compression of the separators also caused radial extrusion of the separator paste. For most PC cells, the extrusion was typically 1.0 mm beyond the perimeter of the cell. The separator extrusion was of comparable magnitude for the SNL-built cells.

Two PC cells with inconsistent thickness changes (PC024 and PC027) were not included in Fig. 16. Cell PC024 was tested at 550°C. A combination of material extrusion at the perimeter and lateral displacement at the interface between the positive electrode and the separator reduced the measured values from those expected. The separator from cell PC027 was compressed considerably more than normal. This deviation may be related to the high current density pulses applied to this cell.

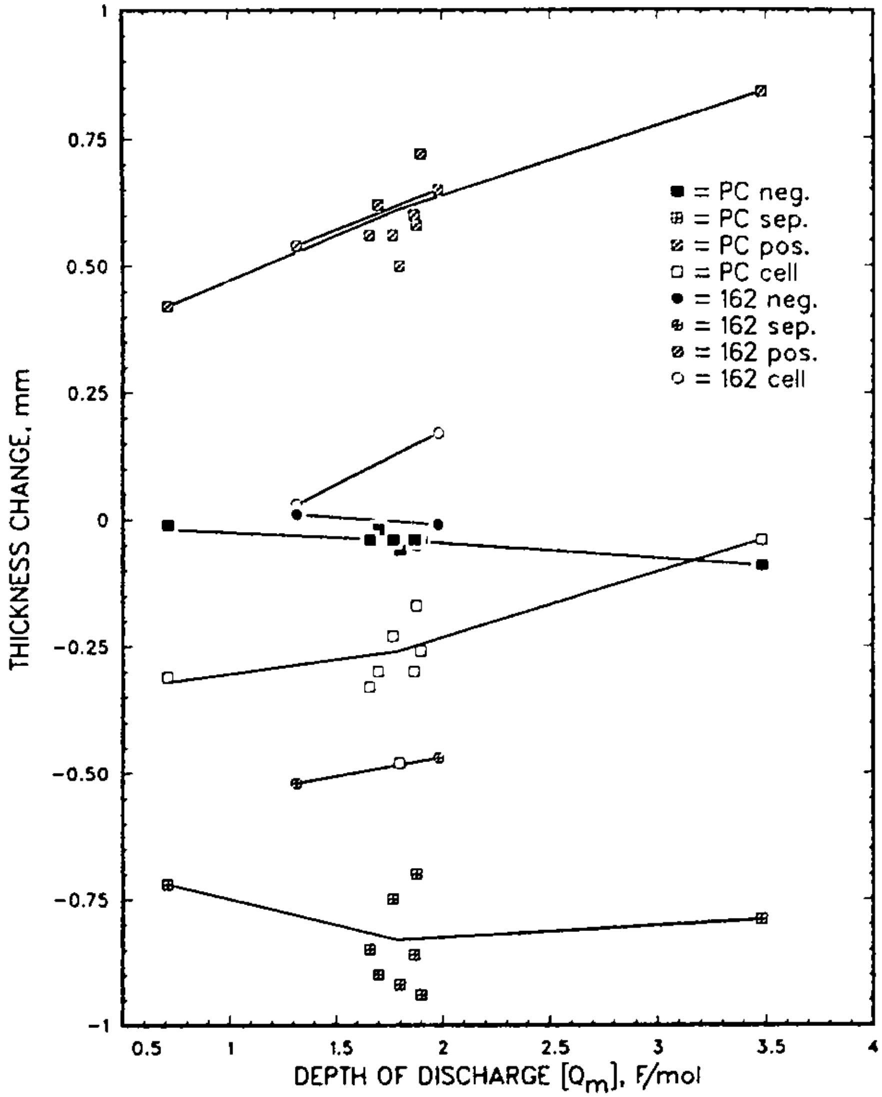

Fig. 16. Changes in Cell and Component Thicknesses as Function of Discharge Level for PC and 162 Series Cells

3.3 Compositional Changes in Electrode Active Materials

Analyses of the phases present in the electrodes from discharged cells provided an additional method of comparing actual cell performance with theoretical behavior. Researchers of Li-Al/FeS_2 secondary cells used a combination of X-ray diffraction (XRD), metallographic, and coulometric techniques to establish the phase transitions that occur during discharge.[6-8] Their findings can be summarized as follows. Complete conversion of FeS_2 to $Li_3Fe_2S_4$ would occur in an ideal cell given a very slow discharge to a level equivalent to 1.5 Q_m. Further discharge to 2.0 Q_m would convert the $Li_3Fe_2S_4$ to Li_2FeS_2 after two reactions, involving the formation and conversion of $Fe_{1-x}S$ and an Li-Fe-S phase that is stable only at elevated temperatures. A complete discharge to 4.0 Q_m would produce the final discharge products of Li_2S and Fe. Discharge of the negative electrode would involve a progressive transformation of $Li_{13}Si_4$ to $Li_{14}Si_6$. Identification and estimation of the phases present were accomplished using optical microscopy. Confirmation of the phase identifications involved XRD analysis of small samples (~2 mm^3) extracted from the electrodes. All the cells showed deviations from ideal kinetics. The available electrolyte, the discharge current density, and the operating temperature were the primary factors influencing the degree of deviation.

3.3.1 Positive Active Materials

3.3.1.1 The SNL Cells

Compositional estimates for the positive electrodes from the SNL-tested cells are expressed as volume percentages in Table 10. Most of the M1 cells were discharged to one of two discharge levels, 0.75 and 1.5 Q_m. For a given discharge level, cells tested at 400°C have more $Li_3Fe_2S_4$ and less Li_2FeS_2 and $Fe_{1-x}S$ than corresponding cells tested at 500°C. At 400°C, cells operated at lower current densities contained more $Li_3Fe_2S_4$. Among the cells discharged to 0.75 Q_m, cell M1-3 (400°C, 12.6 mA/cm^2) was the only cell in which cross sections revealed $Li_3Fe_2S_4$ as the sole discharge product. Cross sections of cells M1-05 (400°C, 25.3 mA/cm^2) and M1-12 (400°C, 50.5 mA/cm^2) revealed that they were the only cells to contain $Li_3Fe_2S_4$ and Li_2FeS_2 as the only discharge products. The cells discharged within the range of 0.37 to 0.75 Q_m at 500°C (M1-21, M1-20, M1-08, M-11, and M1-16) contained $Fe_{1-x}S$ in addition to the other two discharge products. Several cells discharged to 1.5 Q_m developed extreme compositional gradients and contained a band of Li_2S and Fe along the separator interface. Cells in this category included M1-19, M1-15, M1-18, and M1-14.

The distribution of discharge particles within the positive electrodes played a role in the observed electrode expansion as well as the electrochemical performance. In the cells discharged to 0.75 Q_m, the discharged phases were found in the front half of the electrode, and the residual FeS_2 lined the Grafoil collector. In those discharged to 1.5 Q_m, the FeS_2 was found mainly at the circumference and often extruded beyond the separator where it became electrochemically isolated from the electrode proper. In a number of cells (especially cells M1-05, M1-07, M1-16, and M1-14), large areas of FeS_2 particles within the electrode proper were electrochemically isolated because of electrolyte voids along the separator interface. This created an imbalance in localized utilization of active materials. The isolation of internal particles also resulted in the lower-than-average expansion values for these cells. High expansion values in the 1.5-Q_m cell group were found for cells M1-09, M1-18, and M1-19. The first two cells showed no FeS_2 in the examined cross sections, and cell M1-19 "lost" FeS_2 because of misalignment of the cell components.

The photomicrographs in Figs. 17-21 illustrate the progression of phase transformations observed in the M1 cell series. The coarse FeS_2 was estimated to be only 98% pure because of the significant quantity of SiO_2 embedded within the individual FeS_2 particles (Fig. 17). The transformation of the large FeS_2 particles to $Li_3Fe_2S_4$ proceeded rapidly when the starting particle was accessible to electrolyte, because the $Li_3Fe_2S_4$ broke into shard-like fragments as it formed (Fig. 18). The transformation of $Li_3Fe_2S_4$ to Li_2FeS_2 involved the formation of $Fe_{1-x}S$, which incorporates some Li in place

Table 10. Composition of Active Materials in Positive Electrodes from M1, OC, and 162 Cells

Cell Number	Composition, vol %				
	FeS_2	$Li_3Fe_2S_4$	Li_2FeS_2	$Fe_{1-x}S$	Li_2S+Fe
OC-400	100	-	-	-	-
M1-03	45	55	-	-	-
M1-05	50	45	5	-	-
M1-12	40	50	10	-	-
M1-13	35	40	20	-	-
M1-02	5	30	50	15	-
M1-04	20	20	55	5	-
M1-19	15	25	55	5	1
OC-500	100	-	-	-	-
M1-21	65	30	5	-	-
M1-20	60	30	10	1	-
M1-08	40	20	25	15	-
M1-07	40	35	15	10	-
M1-11	35	40	20	5	-
M1-16	50	35	10	5	-
M1-15	10	30	50	5	1
M1-09	-	15	70	15	-
M1-06	2	10	70	20	-
M1-18	-	10	85	-	5
M1-10	5	10	75	15	-
M1-14	20	20	50	5	2
M1-17	1	2	15	2	80
162-19	20	20	55	5	-
162-18	5	5	70	20	-

of Fe, and "W-phase", an Li-Fe-S compound that is stable in the temperature range of cell operation at elevated temperatures. W-phase chemically decomposed during cool down into Li_2FeS_2 and more $Fe_{1-x}S$, producing the microstructure shown in Fig. 19. This morphology was quite prevalent in the cells operated at 500°C. Further reaction converted the $Fe_{1-x}S$ (and W-phase) and broke the Li_2FeS_2 into smaller particles (Fig. 20). At this point, all evidence of the FeS_2 parent particle was lost. In cell M1-17 (Q_m = 2.73 F/mol), continued discharge produced the partial conversion of Li_2FeS_2 to Li_2S and Fe within the body of the electrode (Fig. 21). This sequence of photomicrographs also illustrates the underlying cause for pronounced electrode expansion. In the early stages of discharge, the sharp fragments resisted compaction. A significant increase in the volume fraction of positive-electrode solids occurred only when the rounded Li_2S and fine Fe particles were formed. However, Li_2S, which has a density of 1.66 g/cm^3, is much more voluminous than FeS_2, which has a density of 5.0 g/cm^3; thus, electrode expansion continued.

Fig. 17. Photomicrograph of Coarse FeS_2 Particle Containing SiO_2. (650X)

3.3.1.2 The ANL Cells

Data on the active materials found in the PC cells are compiled in Table 11. As discussed in Sec. 3.2.1, the compression of the thick separators used in these cells made a greater quantity of electrolyte available to the positive electrodes. This factor influenced the morphology more than any other parameter of cell operation.

Most of these PC cells were discharged into the range of 1.66 to 1.90 Q_m and contained about 90 vol % Li_2FeS_2. Some cells in this group contained small percentages of FeS_2 and $Li_3Fe_2S_4$, which were present in

Fig. 18. Photomicrograph of FeS_2 (white) and $Li_3Fe_2S_4$ (light gray). (650X)

isolated regions of the electrode circumference. The discharge products, Li_2S and Fe, were always found at the separator interface. However, these products were also present at the back interface in cells with more than 5 vol % of these phases. Some cells also contained small quantities of $Fe_{1-x}S$ scattered throughout the electrodes. The initial FeS_2 powder size and current density produced no discernible differences in the microstructures observed at this level of discharge. Operation of PC024 at 550°C was the only test variable that introduced a significant change in the microstructure. Cell PC024 contained less Li_2FeS_2 and much more $Fe_{1-x}S$. More importantly, a significant amount (~5 vol %) of metallic iron was present in the central area of the electrode, but no Li_2S could be detected. This rare occurrence suggested that sulfur was being lost at this elevated temperature.

Fig. 19. Photomicrograph of Li_2FeS_2 (light gray) and $Fe_{1-x}S$ (white). (650X)

Cell PC036, which was discharged to 0.71 Q_m, illustrated a significant difference between the PC cells and M1 cells. Unlike the M1 cells that were discharged to roughly equivalent levels (0.75 Q_m), Cell PC036 did not have a segregated positive-electrode microstructure. As shown in Fig. 22, the unreacted FeS_2 and the discharge products were uniformly distributed through the full electrode thickness. Such a microstructure indicates that improved ionic conduction was achieved within the electrode.

3.3.2 Transport of Positive Active Materials into Separator

Burrow et al.[9] used SEM-EDS and Auger electron spectroscopy (AES) to determine that both sulfur and iron migrated during discharge into the

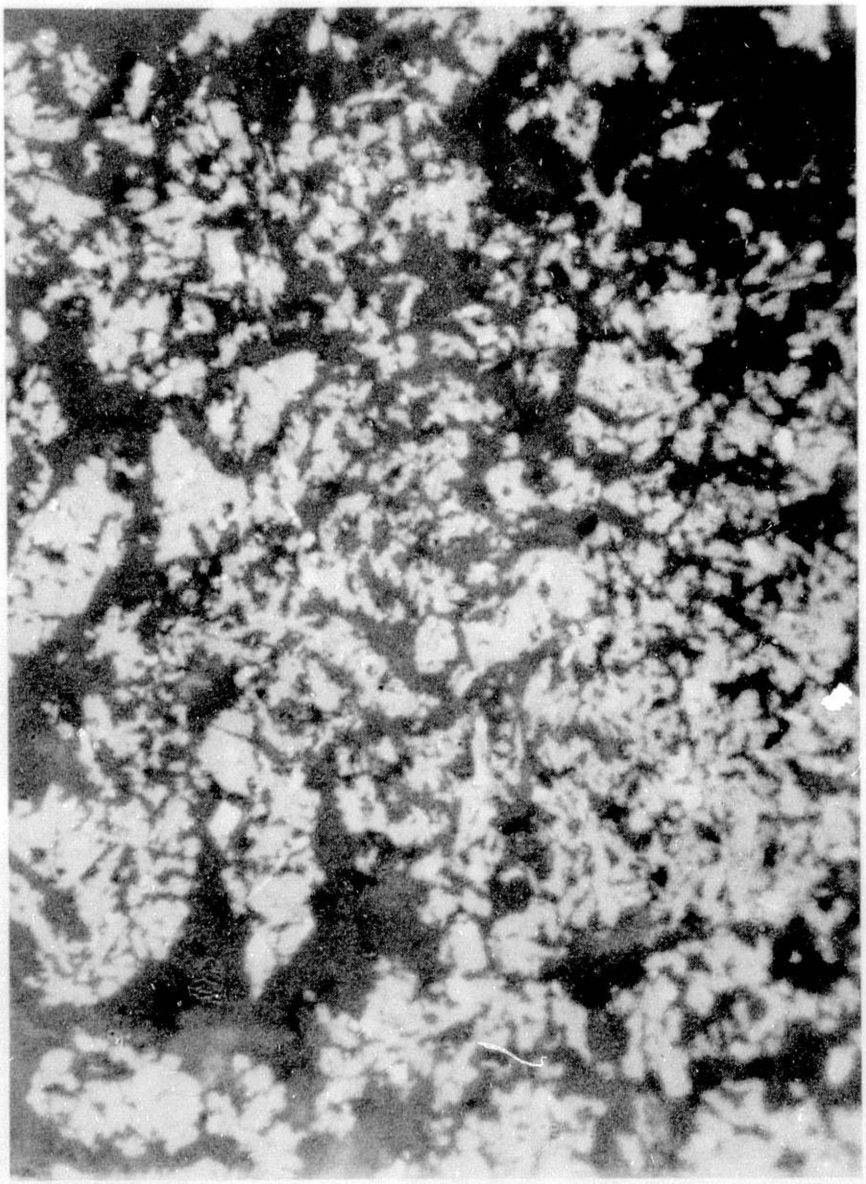

Fig. 20. Photomicrograph of Second Example of Li_2FeS_2 (light gray) and $Fe_{1-x}S$ (white). (650X)

separator of pellet cells. The two elements were found concentrated in overlapping bands that were roughly parallel to the electrode interfaces. They indicated that the thicknesses and positions of these bands were dependent on the discharge current, temperature, and voltage. Longer discharge periods and higher temperatures promoted increased concentrations of both elements within the separator.

Similar temperature-dependent transport of S and Fe was found in the present study. Cells operated at high temperature ($\geq$500°C) developed bands of active material in the separators; cells tested at 450°C had some tendency to develop deposits within the separators; cells operated at 400°C showed no observable active-material deposits.

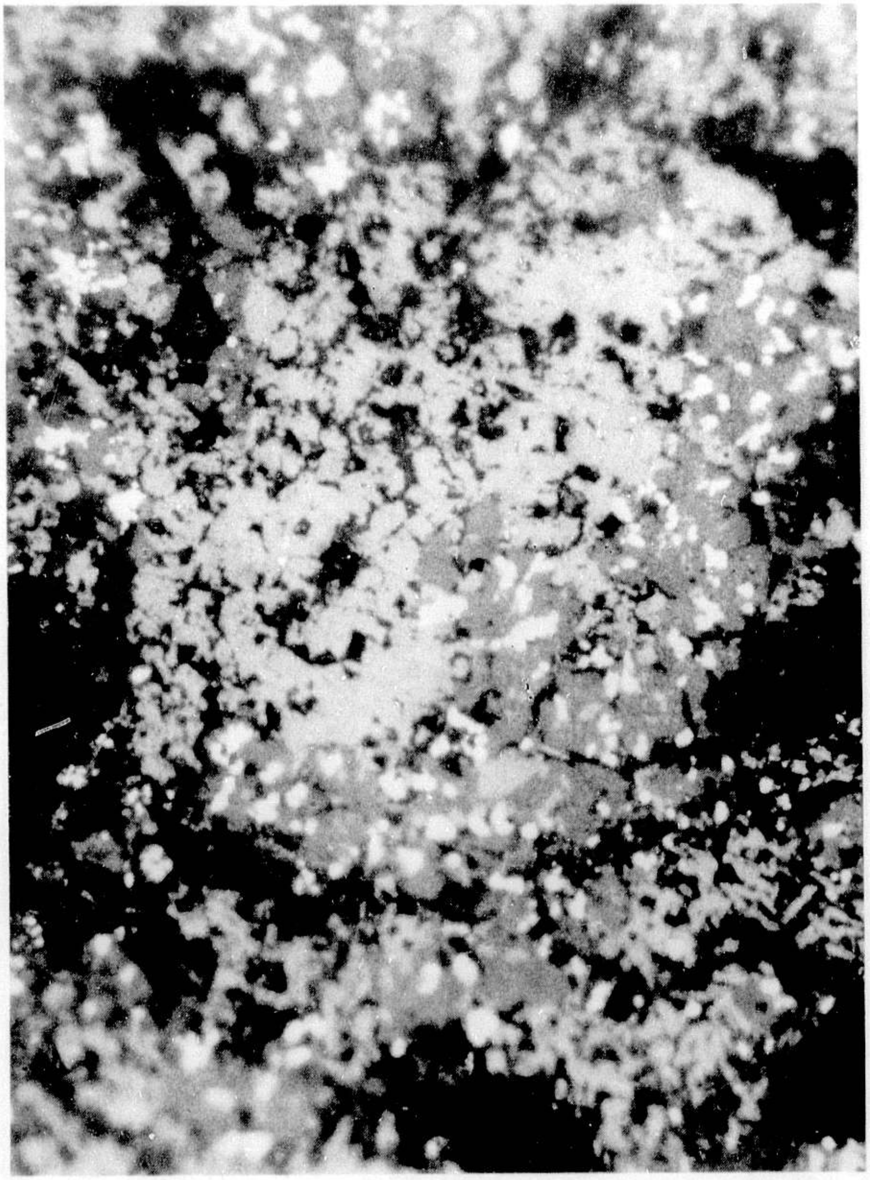

Fig. 21. Photomicrograph of Li_2FeS_2 (light gray), Li_2S (gray), and Fe (white). (650X)

The separators of all the M1 cells tested at 500°C developed bands of light-gray crystals with two exceptions. Cells M1-20 and M1-21 were discharged for the shortest time intervals ($\leq$10 minutes), and no crystals were discernible. For cells that were more deeply discharged (0.75 to 1.5 Q_m), the number of crystals was inversely related to the current density but appeared independent of the depth of discharge. The separators from cells M1-08 and M1-09 (12.6 mA/cm^2) contained the highest--and approximately equivalent--crystal concentrations. X-ray diffraction of a sample carefully removed from the M1-08 separator identified the crystals as Li_2S. Confirming evidence was provided by SEM-EDS; X-ray fluorescence dot maps revealed areas of lower Cl, K, and Mg concentration and increased S concentration in regions of the separator where the crystals were observed optically. For cells M1-08 and M1-09,

Table 11. Composition of Active Materials in Positive Electrodes from PC Cells

Cell Number	Composition, vol %				
	FeS_2	$Li_3Fe_2S_4$	Li_2FeS_2	$Fe_{1-x}S$	Li_2S+Fe
PC036	50	30	18	2	-
PC019	2	1	87	2	8
PC035	2	-	91	-	7
PC014	1	-	90	1	8
PC015	3	1	86	2	8
PC009	-	-	5	-	95
PC012	1	1	90	-	8
PC024	-	-	80	15	5[a]
PC026	-	-	97	-	3
PC025	2	-	95	-	3
PC027	1	-	84	-	15

[a] Metallic iron only; no Li_2S present.

the crystals occupied ~10% of the separator cross section and were aligned into two rows, as shown in Fig. 23. The distance of the inner row of Li_2S from the positive interface of both cells was 20 to 30% of the separator thickness, and the outer band was 50 to 60% away from this interface. At discharge rates higher than 12.6 mA/cm², both the number and size of the Li_2S crystals decreased. For cells M1-15 and M1-17 (discharge rate $\geq$75 mA/cm²), the separators contained less than 1% Li_2S scattered in the middle of the separator.

A phenomenon related to Li_2S formation was the presence of one or two discoloration bands within the affected separators. These bands were visible in polarized light. In separators with double crystal rows, the bands of discoloration coincided with the crystals (Fig. 24). The band closer to the negative electrode was black (upper band in Fig. 24), and the band near the positive electrode was red-orange (lower band in Fig. 24). In separators with a single row of Li_2S crystals, only the black band was present. Examination by SEM-EDS indicated that the black discoloration was due to a low concentration of iron. The source of the red-orange coloration has not been determined.

As mentioned previously, Li_2S crystals were not seen in cells M1-20 and M1-21; however, these two cells did have black bands of discoloration similar to the ones found in other cells tested at 500°C. Apparently, optically observable crystals of Li_2S could not develop during short periods of operation, although the migration of cathode materials had been under way. The inverse dependence of Li_2S formation and iron discoloration on the discharge current for the more deeply discharged cells was another indicator of the time dependence of this transport process. However, the comparable levels of crystallization and discoloration (at a given current density) found for cells discharged to either 0.75 or 1.5 Q_m suggested that transport becomes negligible beyond a certain discharge level.

Fig. 22. Photomicrograph of FeS_2 Particles (light) and Discharge Products (dark) Randomly Distributed through Positive Electrode of Cell PC036. (Areas containing the electrolyte-MgO mixture appear hazy white.) (130X)

The temperature dependence of active-material migration was very pronounced. None of the cross sections from the group of 400°C cells showed Li_2S formation or iron discoloration. Low levels of Li_2S and faint discoloration bands were observed in some of the 450°C group of cells, but only the cross

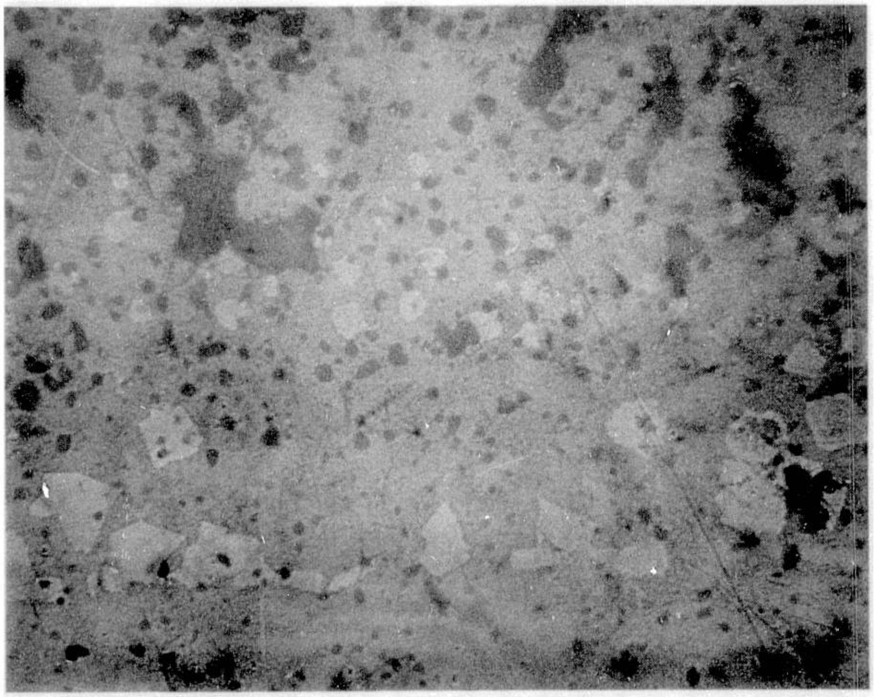

Fig. 23. Double Rows of Li_2S Crystals Found in Separator from Cell M1-08. (200X)

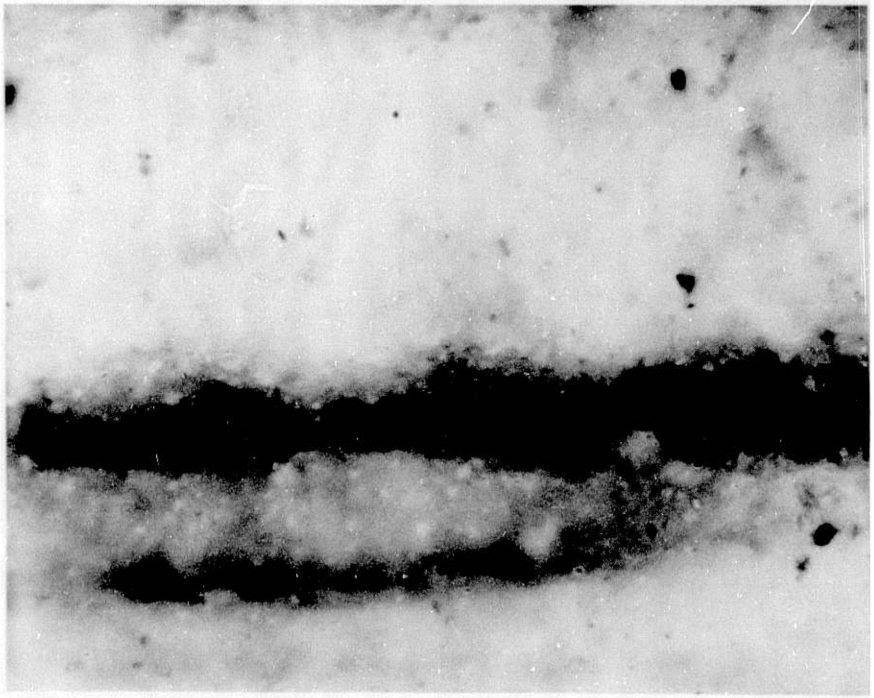

Fig. 24. Same Area as in Fig. 23 under Polarized Light. (200X)

section through cell PC035 (50 mA/cm^2) revealed clear evidence of both phenomena. The data for the 500°C group of cells have already been discussed. One of the more surprising findings was made for the cell tested at 550°C. Cell PC027 contained small particles (<5 μm) of metallic iron in addition to Li_2S crystals. (The separator was also discolored.) The direct correlation between temperature and the severity of active-material migration suggested that the process is controlled by the kinetics of FeS_2 reduction.

3.3.3 Negative Active Materials

The negative electrodes from all the tested cells showed little change from the starting electrode morphology. The discharge product, $Li_{14}Si_6$, was optically indistinguishable from the starting compounds of $Li_{13}Si_4$. A slight difference was noted in the particles of cells discharged beyond about 1 Q_m. The reaction of the Li-Si particles from these cells had progressed sufficiently to show some visible breakdown of the sharp, well-defined surfaces.

X-ray diffraction was used to qualitatively establish the relative amounts of the two Li-Si phases in selected cells. For cell OC-500, $Li_{13}Si_4$ was the major phase, but minor amounts of $Li_{14}Si_6$ were also present. In cells discharged to 1.5 Q_m, the relative line intensities for these compounds were approximately reversed. Cell M1-15 was the only sampled electrode that showed a detectable gradient. This cell was discharged at a high current density (75.8 mA/cm^2) and had a higher $Li_{14}Si_6/Li_{13}Si_4$ ratio in the front half of the electrode than in the back half.

3.4 Electrolyte Distribution and Compositional Gradients

The quantity of electrolyte within the cell components changes during heatup as a result of the starved-electrolyte design. This design requirement also accentuates local deviations from the starting LiCl-KCl eutectic composition when cells are discharged. For the test cells, these mass and compositional shifts were frozen in place by the rapid cool down. To analyze these changes, selected cells were probed across their full thicknesses. Once again, separator thickness and applied pressure played a major role in shaping these electrolyte changes.

3.4.1 Measurement of Electrolyte Distribution

The analysis technique consisted of collecting X-ray spectra at multiple locations along a line across a cell section. The SEM image was varied between 500 and 2000X, depending upon the component thickness. Generally, three to four spectra were collected for each electrode. The number of spectra taken for the separators varied from three to six because of the large thickness variations for these components. The electrolyte content for a sampled area was determined by taking the ratio of the counts in the chlorine peak to the counts for the entire spectrum. This value was then divided by the ratio of chlorine counts to spectrum counts for a LiCl-KCl eutectic standard. Repeated measurements of the standard were averaged, resulting in a value of 0.44 for the denominator ratio. Each "resultant double ratio" value was correlated with the midpoint of the sampled area to determine trends in electrolyte distribution. The double-ratio value provided a direct way of making comparisons between spectra collected from the same type of component; however, comparisons between values from different components are not as accurate because the different elements (Fe, S, Mg, and Si) in these components influenced the total counts for a spectrum.

Analysis of the spectra collected from 18 cells revealed that major differences in the electrolyte content for a given cell component occurred between cell groups (PC, M1, and 162). To minimize sampling variability, the double ratio values for a given component in a given cell were averaged. These averages for chlorine content were condensed further by determining mean values for each type of component within a cell group.

Table 12 lists these mean values for the chlorine peaks of the M1, 162, and PC cell groups. The electrolyte content in the negative electrodes was quite similar for the 162 and PC cells but considerably lower for the M1 cells. Our interpretation of this finding is that the thicker separators used in the 162 and PC cells provided a greater reservoir from which the initially "dry" negatives electrodes could extract electrolyte through capillary action. The somewhat higher mean chlorine value for the PC cells may reflect the influence of the higher applied pressure. For the positive electrodes, the M1 and 162 cells have similar mean values, which fall considerably below that of the PC cells. This finding is presumed to be a result of the higher applied pressure; the greater mechanical force pushed more of the separator mix into the comparatively open structure of the positive electrode. The separators for these three groups of cells would be expected to show similar contents of electrolyte; however, the value for the 162 cells fell far short of those for the other two groups. Microscopy provided an insight into this discrepancy. During cool down, all of the separators developed cracks that continued to widen into electrolyte-free fissures. These fissures were very pronounced in the separators of the 162 cells and would have reduced the proportion of chlorine and magnesium counts with respect to total background radiation. As a result, the double-ratio values would have understated the chlorine content of the 162 cells with respect to the other cells.

Analysis of individual chlorine values revealed one additional trend followed by virtually all of the cells. The electrolyte content for the negative electrodes consistently declined by a factor of two from its maximum value near the separator to a minimum at the back. For cell M1-18, which used a 1.5-g electrode, the minimum occurred in the middle and held constant through the back half. The only cell to deviate from this pattern was cell PC027, which maintained a nearly constant electrolyte level. This cell also had nearly twice the normal separator compression found in its cell group.

Other cell parameters, such as temperature, current density, depth of discharge, and FeS_2 particle size, had no discernible influence on the final electrolyte content within a cell. The effect of particle size (cells PC014, PC026, PC025, and PC027) could have been masked by the residual void areas present in the positive electrodes. These electrodes showed the greatest fluctuation in individual chlorine values because of this factor.

Table 12. Relative Quantity of Electrolyte within Different Components for Three Cell Groups[a]

Cell Group	Number of Cells	Positive Electrode Mean	Positive Electrode Std. Dev.	Separator Mean	Separator Std. Dev.	Negative Electrode Mean	Negative Electrode Std. Dev.
M1	8	0.24	0.04	0.75	0.16	0.16	0.06
162	2	0.25	0.08	0.62	0.14	0.26	0.04
PC	8	0.34	0.06	0.80	0.10	0.29	0.05

[a] Based on SEM-EDS analysis of the chlorine using the double-ratio method. See text.

3.4.2 Measurement of Electrolyte Compositional Gradients

The collected SEM-EDS spectra were also used to study the gradients in electrolyte composition that developed within these cells. A software program entitled "ZAP" was used to convert the raw potassium- and chlorine-peak counts into estimates of the atomic percentages. (Lithium cannot be detected by SEM-EDS). Ideally, the K/Cl ratio is 0.418 for LiCl-KCl eutectic. The K/Cl ratios derived from these measurements showed wide deviations from this value. Unfortunately, not all the variation was genuine. Exposures to air prior to sample coating and insertion into the SEM port would increase the measured surface K/Cl values as a result of reactions with moisture. (Air-exposure studies on the eutectic standard confirmed this point.) As a result, quantitative comparisons were not possible, but qualitative ones could be made.

The predominant trend found in the K/Cl profiles can be described as follows. For cells discharged to 0.75 Q_m and beyond, the K/Cl ratio was at a maximum in the back half of the positive electrode. The ratio then declined in the front half of this electrode and continued to decline into the separator. The minimum, corresponding to a LiCl-rich composition, occurred within the separator or at the negative-electrode interface. The K/Cl ratio then increased through the remainder of the negative electrode and reached a value near that of the eutectic. The K/Cl profile found for Cell 162-19 was representative of this trend and is shown in Fig. 25.

Differences in this basic profile were discernible between the cell groups. The minimum in four M1 cells (M1-02, M1-09, M1-10, and M1-12) occurred at the negative-electrode interface. In the other M1 cells (M1-08, M1-11, M1-15, and M1-18), the minima were in the separator, but the K/Cl values were still low at this interface. For the PC cell group, the difference between the maximum and minimum values tended to be smaller, and three cells (PC014, PC015, and PC027) had relatively flat profiles through the entire thickness of the negative electrode. The smoothing effect noticed for the PC cell group could be due to a greater quantity of electrolyte within the electrodes of these cells.

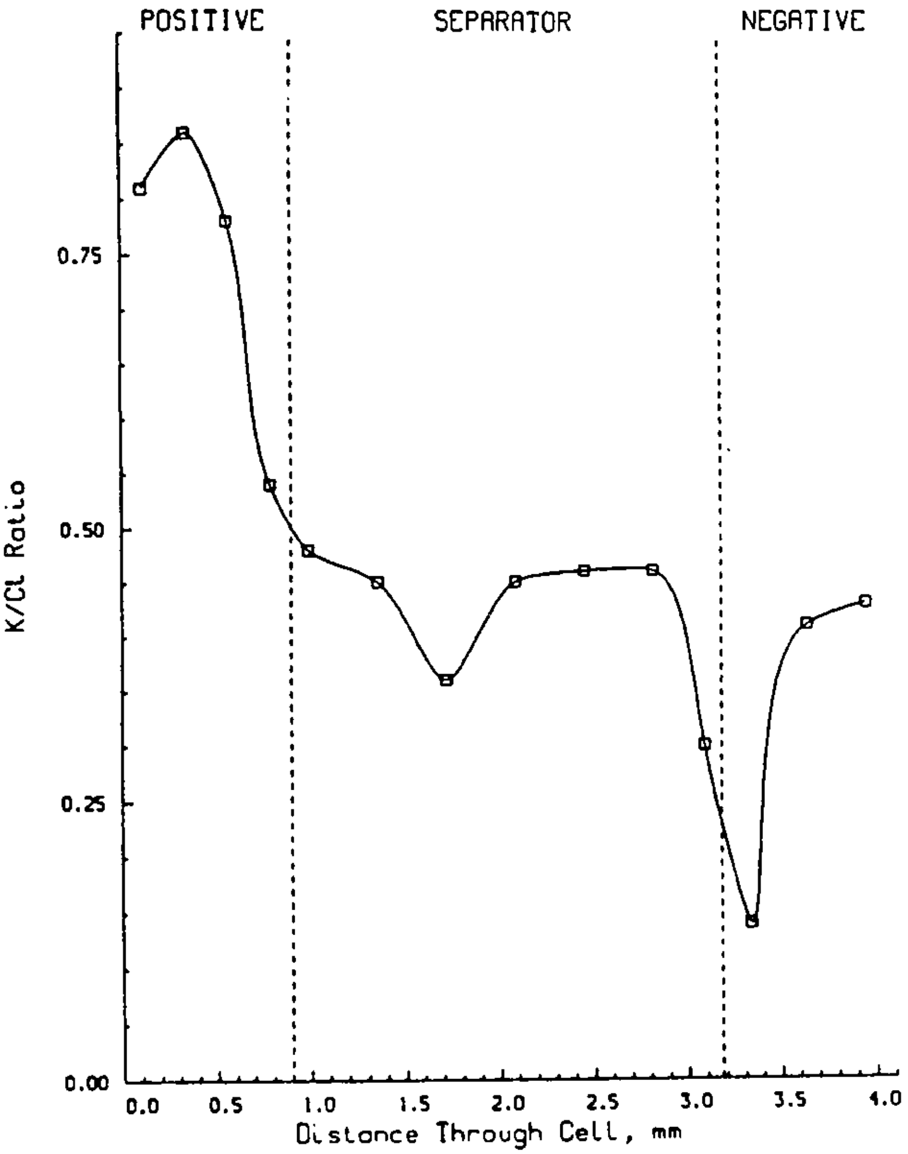

Fig. 25. Variation in Ratio of Potassium to Chlorine as Function of Location within Cell 162-19

Cell PC036 (Q_m = 0.71 F/mol) was of special interest because its discharge was terminated near the point of highest resistance within the positive electrode. A likely cause for the higher resistance was the K/Cl gradient in the electrolyte. In cell PC036, the maximum value for the K/Cl ratio occurred at the interface of the positive electrode with the separator. This suggested that the gradient had not yet established its steady-state form. Future studies on cells such as M1-20 and M1-21 (Q_m = 0.418 and 0.375 F/mol, respectively) may determine how the gradient develops into its characteristic form.

Confirmation of the compositional gradients was obtained from other examination techniques. The XRD samples of electrode materials invariably showed much higher KCl concentrations in the positive electrodes and comparable concentrations of KCl and LiCl in the negative electrodes.

3.5 Concluding Observations on the Post-Test Examinations

On a microstructural basis, the key determinants of cell performance were the distribution of electrolyte within the electrode and the expansionary action of the phase transitions that occurred in the positive electrode. The less-than-ideal shape of the reaction products that formed in the early stages of discharge prevented dense packing and minimized interparticle contact. The electrolyte content per unit volume of electrode also decreased as a result of the electrode expansion. Thicker separators and higher applied pressures worked in unison to offset electrolyte deficiencies by making more electrolyte available to the electrode beds. As a result, discharge of the positive electrode occurred more uniformly throughout the full electrode thickness in the cells that incorporated these features. The semi-quantitative analysis of electrolyte distribution confirmed the improvement in electrolyte content. The moderation noted in electrolyte compositional gradients also reflected the benefits of improved electrolyte distribution.

The post-test findings for the effects of other test parameters on cell performance were less conclusive for several reasons. Time constraints permitted examinations of a limited number of cells. Also, normal variations would be expected among different cross sections through a given cell. Finally, the influence of secondary parameters, such as FeS_2 particle size and discharge current density, appear relatively small in comparison with that of primary parameters.

4 RECOMMENDATIONS

The following recommendations for further investigation of the Li-Si/FeS_2 cell are made:

1. Analyze further the currently available data and test new electrode samples. To date, 82 successful cell testings have been completed. The generated data base contains about 250,000 pieces of information. A complete analysis of the huge data base has not been possible within the relatively short time available.

2. Investigate the effect of additives in the positive electrode. Based on the presented results, we believe that further evaluation of graphite powder additive is expedient. Molybdenum powder additive may turn out to be even more effective than graphite. Experimentation with NiS_2 and/or CoS_2 additives is recommended as well.

3. Investigate the role of the composition and the relative quantity of the electrolyte. Electrochemical measurements in accordance with the post-test investigations have revealed (only semi-quantitatively so far) the importance of the ratio of electrolyte volume fraction to the loading density and also the electrolyte distribution within the cell sandwich. Increasing the electrolyte volume within the constraints of the mechanical properties of the pellets and fine-tuning of electrolyte composition will increase cell performance. The present work indicates that adjustments in the electrolyte composition used for the separator pellets should be explored. Also, the effects of new electrolyte compositions, e.g., the low-melting LiCl-LiBr-KBr and the all-Li^+-cation electrolyte (LiF-LiCl-LiBr), should be investigated.

4. Determine the pressure applied to a cell stack during discharge of a thermal battery. Preliminary experiments completed so far have shown the pronounced effect of pressure on cell performance. The component thicknesses in the SNL-supplied thermal batteries should be measured and compared with the pressure-dependent changes in thickness determined for individual cells. This would be an important step in determining the relevant pressure range for actual operating conditions.

5. Apply the Integrated Measuring and Modeling Method. This method, which has been developed at ANL for battery-performance optimization, should be considered for application in Li-Si/FeS_2 primary cell development as a further task in the collaboration of SNL and ANL.

These recommendations are justified by the results of the experiments reported herein. The recommendations cover areas of research that offer improvement in cell performance. The completion of all these subtasks, however, requires an effort of many man-years. Therefore, decision is required concerning the volume of future work and the setting of priorities for immediate efforts.

REFERENCES

1. L. Redey and J. A. Smaga, Argonne National Laboratory, unpublished information (1986).

2. Argonne National Laboratory, unpublished information (1985).

3. L. Redey, D. R. Vissers, J. Newmann, and S. Higuchi, Electrode Characterization of Li-Al/FeS Cells by Voltage-Loss Investigation, Proc. Symp. Porous Electrodes: Theory and Practice, ed. H. Maru et al., The Electrochemical Soc., Proc. Vol. 84-8, Pennington, NJ, p. 322 (1984).

4. J. E. Battles, F. C. Mrazek, and N. C. Otto, Post-Test Examinations of Li-Al/FeS_x Secondary Cells, Argonne National Laboratory Report ANL-80-130 (December 1980).

5. F. C. Mrazek, Microscope 31, 235 (1983).

6. A. E. Martin, The Li-Fe-S Phase Diagram, Argonne National Laboratory Report ANL-78-94, pp. 167-168 (November 1978).

7. A. E. Martin and Z. Tomczuk, Chemistry of FeS_2 Electrodes, Argonne National Laboratory Report ANL-79-39, pp. 71-73 (May 1979).

8. Z. Tomczuk, B. Tani, N. C. Otto, M. F. Roche, and D. R. Vissers, J. Electrochem. Soc. 129, 925 (1982).

9. B. J. Burrow, K. W. Nebesny, N. R. Armstrong, R. K. Quinn, and D. E. Zuravski, J. Electrochem. Soc. 128, 1919 (1981).

Distribution for ANL-87-6

Internal:

J. E. Battles
I. D. Bloom
A. A. Chilenskas
C. C. Christianson
W. H. DeLuca
D. C. Fee
J. E. Harmon
T. D. Kaun
J. Lee
J. F. Miller
F. C. Mrazek
T. P. Mulcahey
P. A. Nelson
L. Redey (9)
J. A. Smaga
M. J. Steindler
Z. Tomczuk
A. F. Tummillo
R. Varma
D. R. Vissers
C. Woodcock
ANL Patent Dept.
ANL Contract File
ANL Libraries
TIS Files (5)

External:

DOE-TIC, for distribution per UC-94cb (206)
Manager, Chicago Operations Office, DOE
Chemical Technology Division Review Committee Members:
  S. Baron, Brookhaven National Laboratory, Upton, NY
  T. A. Milne, Solar Energy Research Institute, Golden, CO
  L. Newman, Brookhaven National Laboratory, Upton, NY
  J. B. Wagner, Arizona State University, Tempe, AZ
  R. G. Wymer, Oak Ridge National Laboratory, Oak Ridge, TN
  T. L. Brown, U. of Illinois, Urbana, IL
J. Ambrus, Naval Surface Weapons Center, Silver Spring, MD
A. Andazola, Sandia National Laboratories, Albuquerque, NM
W. A. Averill, Sandia National Laboratories, Albuquerque, NM
G. Barlow, Gould Inc., Rolling Meadows, IL
A. A. Benderly, Potomac, MD
D. A. Benish, Hughes Aircraft Company, Canoga Park, CA
W. S. Bishop, Aero Propulsion Laboratory, Wright-Patterson AFB, OH
F. Butler, Naval Sea Systems Command, Washington, DC
E. J. Cairns, Lawrence Berkeley Laboratory, Berkeley, CA
J. Degruson, Eagle-Picher Industries, Inc., Joplin, MO
L. DeJonghe, Lawrence Berkeley Laboratory, Berkeley, CA
C. Dymek, U.S. Air Force Academy, Colorado Springs, CO
K. L. Englander, Naval Ordnance Station, Indian Head, MD
J. K. Erbacher, Wright-Patterson AFB, OH
S. Geddes, Ratheon Company, Bedford, MA
F. Gibbard, Power Conversion, Inc., Elmwood Park, NJ
J. A. Gilbert, Sandia National Laboratories, Albuquerque, NM
N. A. Godshall, Sandia National Laboratories, Albuquerque, NM
P. E. Grayson, Eagle-Picher Industries, Joplin, MO
S. Gross, Boeing Aerospace Company, Seattle, WA
R. A. Guidotti, Sandia National Laboratories, Albuquerque, NM (3)
R. Hudson, Eagle-Picher Industries, Inc., Joplin, MO
A. K. Jacobson, Sandia National Laboratories, Albuquerque, NM
C. Johnson, Boeing Aerospace Company, Seattle, WA
J. Kavandi, Boeing Aerospace Company, Seattle, WA
A. R. Landgrebe, Energy Storage and Distribution Div., USDOE, Washington, DC
B. Larrick, Naval Surface Weapons Center, Silver Spring, MD
F. P. Lasky, Sandia National Laboratories, Albuquerque, NM
R. S. Lazar, Naval Underwater Systems Center, Newport, RI

Arthur D. Little, Inc., Cambridge, MA
N. J. Magnani, Sandia National Laboratories, Albuquerque, NM
R. A. Marsh, Wright-Patterson AFB, OH
J. W. McCauley, Army Materials and Mechanics, Watertown, MA
F. McLarnon, Lawrence Berkeley Laboratory, Berkeley, CA
M. H. Miles, Naval Weapons Center, China Lake, CA
C. E. Mueller, White Oak Laboratory, Silver Spring, MD
M. F. Murphy, Naval Sea Systems Command, Washington, DC
J. T. Nelson, Harry Diamond Labs, Adelphi, MD
J. S. Newman, University of California, Berkeley, CA
D. A. Nissen, Sandia National Laboratories, Albuquerque, NM
R. Nolan, Naval Weapons Center, China Lake, CA
N. Otto, Science Applications International, Schaumburg, IL
K. K. Press, SAFT America, Cockeysville, MD
F. W. Reinhardt, Sandia National Laboratories, Albuquerque, NM
D. Rosenlof, Naval Weapons Center, China Lake, CA
H. J. Saxton, Sandia National Laboratories, Albuquerque, NM
G. L. Scharrer, Sandia National Laboratories, Albuquerque, NM
L. A. Schaum, Hughes Aircraft Company, Tucson, AZ
J. Q. Searcy, Sandia National Laboratories, Albuquerque, NM
F. Smith, Eagle-Picher Industries, Inc., Joplin, MO
R. Spencer, Eagle-Picher Industries, Inc., Joplin, MO
F. Tepper, Catalyst Research Corporation, Baltimore, MD
C. W. Tobias, University of California, Berkeley, CA
R. D. Wehrle, Sandia National Laboratories, Albuquerque, NM
C. S. Winchester, Catalyst Research Corporation, Baltimore, MD
P. Wong, Army Materials and Mechanics, Watertown, MA
R. C. Zaluga, Sandia National Laboratories, Albuquerque, NM
A. Attewell, Royal Aircraft Establishment, Farnbrough, ENGLAND
I. Faul, Royal Aircraft Establishment, Farnbrough, ENGLAND
L. Pearce, Admiralty Marine Tech. Establishment, Pouge, Dorset, ENGLAND
P. Ruetschi, Leclanche, S. A., Yverdon-Les-Bains, SWITZERLAND